Exploring the Influence of Size-Related Factors on Geocell-Reinforced Soil Response using Coupled Continuum-Discontinuum Analysis

Haibo Wang
Graduate student, State Key Laboratory of Ocean Engineering, Shanghai Key Laboratory for Digital Maintenance of Buildings and Infrastructure, School of Naval Architecture, Ocean & Civil Engineering, Shanghai Jiao Tong University, Shanghai 200240, China
Email: whb1994@sjtu.edu.cn

Ge Gao, PhD
Assistant Professor, State Key Laboratory of Ocean Engineering, Shanghai Key Laboratory for Digital Maintenance of Buildings and Infrastructure, School of Naval Architecture, Ocean & Civil Engineering, Shanghai Jiao Tong University, Shanghai 200240, China
(Corresponding author)
Email: gaoge@sjtu.edu.cn

Mohamed A. Meguid, PhD, PEng
Professor, Department of Civil Engineering
McGill University, 817 Sherbrooke St. W., Montreal, QC, H2A 0C3
Email: mohamed.meguid@mcgill.ca

Yi Pik Cheng, PhD
Associate professor, Department of Civil, Environmental and Geomatic engineering
University College London, Gower Street, London, WC1E 6BT
Email: yi.cheng@ucl.ac.uk

Lulu Zhang, PhD
Professor, State Key Laboratory of Ocean Engineering, Collaborative Innovation Center for Advanced Ship and Deep-Sea Exploration, Shanghai Key Laboratory for Digital Maintenance of Buildings and Infrastructure, School of Naval Architecture, Ocean & Civil Engineering, Shanghai Jiao Tong University, Shanghai 200240, China
Email: lulu_zhang@sjtu.edu.cn

Abstract:

Size-related factors, such as the dimensions and cell count of geocell, play a crucial role in determining the effectiveness of soil reinforcement. In this study, a 3D coupled framework that leverages the strengths of both continuum and discontinuum methods was developed to investigate the influence of pocket size and multi-cell configuration on geocell-reinforced soils. To unveil the impact of size-related factors on soil-geocell interactions, reinforced soils containing various geocell configurations (single large-sized cell, multiple small-sized cells), as well as geocell-free soils subjected to increasing levels of confining pressure were extensively examined. This thorough investigation aimed to establish correlations between macroscopic responses and underlying micromechanical mechanisms. Our findings revealed that the presence of the geocell not only enhances the densification of interparticle contacts and reduces the number of floating particles that contribute minimally to load support, but also facilitates the concentration of force chains within the geocell structure. This leads to an increase in elastic stiffness along the loading axis. These observations highlight that the geocell's confining mechanism enhances both the load-carrying capacity and the infill rigidity, thereby preventing lateral soil spreading. In essence, the geocell serves to increase the soil's ability to withstand load and maintain its structural integrity laterally.

Keywords*:* Geosynthetics; Geocell-reinforced soil; Size-related factors; Coupled continuum-discontinuum method; Microscopic characterization

1 Introduction

With the rapid evolution of the synthetic material industry, geosynthetics have emerged as the fourth essential construction material, following cement, steel, and timber in civil engineering (Xu, 2021). Geocells, three-dimensional expanding cellular polymer products, find extensive application in subgrades, foundations, railways, retaining walls, slopes, pavements, and more (Hegde, 2017; Mahgoub and El Naggar, 2020; Sitharam et al., 2020; Amiri et al., 2023). A concerted effort has been directed towards achieving more economical, efficient, and secure geocell-reinforced structures (Huang et al., 2023; Zhao et al., 2023).

The effectiveness of geocell reinforcement is inherently tied to the geometry, manufacturing material of the geocell, properties of the infill material, and more (Sheikh and Shah, 2021). Notably, the cell's opening size plays a pivotal role in the design and application of geocell-reinforced infrastructures. This size factor primarily encompasses the size and number of cells. While larger cell pockets reduce geocell quantities and costs, they can compromise the reinforcement effect (Biswas and Krishna, 2017; Sawada et al., 2023). Nevertheless, financial and practical constraints limit large-scale field experiments, necessitating size or quantity reduction to suit laboratory setups.

Thus, extensive laboratory experiments have explored the influence of size factors on geocell confinement and reinforcement mechanisms. Triaxial compression tests conducted by Rajagopal et al. (1999) examined geocell-reinforced soils with interconnected and single cells, finding that just three interconnected cells in the lab could emulate the response of multiple interconnected cells in a geocell reinforcement layer. Additionally, the study underscored that

geocell reinforcement imparts cohesive strength even to cohesionless soils. Emersleben and Meyer (2009) investigated the impact of adjacent cell count through radial load tests, revealing that an increased cell count leads to better restraint of infill material, greater earth resistance, and higher horizontal pressure.

Through static plate loading tests, Pokharel et al. (2010) noted that multiple-cell reinforcement enhances soil performance, surpassing single geocell reinforcement in stiffness and ultimate bearing capacity. Chen et al. (2013) conducted a series of triaxial compression tests on geocell-reinforced soils, with particular attention to size factors. Results highlighted that multiple cells are more constrained than a single cell, significantly affecting the strength of the reinforced soil. The researchers also pointed out that increased confining pressure reduces the reinforcing effect, suggesting higher effectiveness at lower confinement. Dash (2020) performed physical model tests to elucidate size factors' influence on geocell-reinforced foundations under strip loading. They discovered that as cell size increases, confinement decreases, allowing soil to deform more, demonstrating size-related deformation effects. These studies collectively established macro-level principles governing geocell reinforcement concerning size factors. Yet, they fall short of providing real-time insight into the strength, deformability, and underlying mechanisms of geocell-soil interaction.

Relative to experimental studies, numerical analyses have gained prominence in studying geosynthetic-reinforced soil systems due to their superiority in reproduction and visual representation of soil-structure interacting process (Ngo et al., 2019; Sukkarak et al., 2021a; Bergado et al., 2022). Two main numerical methodologies are utilized: continuum and

discontinuum methods. Continuum-based methods, such as the finite element method (FEM) and finite difference method (FDM) (Jirawattanasomkul et al., 2018, 2019), soils are modeled using solid element. Similarly, the geocell can also be modeled by solid element (Leshchinsky and Ling, 2013a; Leshchinsky and Ling, 2013b; Biabani et al., 2016; Arias et al., 2020; Nayyar and Sahu, 2021) or simplified planar structural elements (Hegde and Sitharam, 2015a; Satyal et al., 2018; Ari and Misir, 2021; Gedela and Karpurapu, 2021; Sheikh et al., 2021). These methods excel in simulating large-scale models efficiently but do not fully capture the granular nature of soil (Grange and Salciarini, 2022).

In contrast, discontinuum methods, especially the discrete element method (DEM), have been extensively used for soil-geostructure studies (Cundall and Strack, 1979). DEM represents soil and geocells with discrete particles, though modeling complex geocell geometries requires a substantial number of bonded grains (Ngo Ngoc et al., 2016; Liu et al., 2018, 2020b). However, modeling geocells as bonded particles lacks realism and efficiency due to their continuous and homogeneous synthetic material nature. To accurately simulate geocell-reinforced soils' mechanical response to external loading, a methodology representing the distinct properties of both geocell and granular soil is essential.

Consequently, this study employs a coupled continuum-discontinuum framework capable of capturing the differing characteristics of soils and continuous geocell material. This methodology, successfully applied and validated in geosynthetic-reinforced soils (Tran et al., 2013, 2015), is constructed based on an experimental program (Chen et al., 2013) and enhanced with geocell configurations accounting for size factors. The specific aims of this

study are as follows:

To investigate how size-related aspects, such as the size of individual cells and the use of multiple cells, affect the response of geocell-reinforced soil;

To assess and compare the effectiveness of different geocell sizes in improving the shear strength of soil;

To explore the impact of size factors on the deformation and mechanical behavior of geocell-reinforced soil. This includes an analysis of micromechanical elements such as the evolution of coordination and redundancy numbers, the development of elastic stiffness, and the characterization of microstructures within various geocell size configurations.

2 Numerical model

2.1 Coupling mechanism of continuum and discontinuum model

The continuum-discrete coupling scheme has been implemented in the FDM software FLAC3D and the DEM software PFC3D (Itasca Consulting Group, 2022a). The sand has been modeled using the ball object in DEM, while the geocell has been simultaneously replicated using the zone object in FDM, based on their respective material properties. As a result, the fundamental principle of the FDM-DEM coupling method is to establish a bridging connection between the ball and the zone. However, direct interaction between the ball and zone does not occur. Therefore, interfacial coupling walls have been introduced on the surface of the zone to mediate the interaction between the balls and zones, as illustrated in Fig. 1. In the DEM, the wall object is composed of triangular facets that together form a spatial surface. Movement and forces are transmitted via the vertices of these triangular facets within the

coupling wall. The contact location P_c of a ball-facet interaction is determined by Eq. (1). As illustrated in Fig. 1 (a), $\boldsymbol{P_b}$ is the centroid of the ball, $\boldsymbol{P_f}$ is the point on the facet with the shortest distance d to $\boldsymbol{P_b}$, R denotes the ball radius, g_c is the contact gap, and $\boldsymbol{n_c}$ indicates the normal direction of contact.

$$\begin{cases} \boldsymbol{P_c} = \boldsymbol{P_b} + \left(R + \dfrac{g_c}{2} \right) \boldsymbol{n_c} \\ g_c = d - R \\ \boldsymbol{n_c} = \dfrac{\boldsymbol{P_f} - \boldsymbol{P_b}}{\boldsymbol{P_f} - \boldsymbol{P_b}} \end{cases} \tag{1}$$

On account of only vertex being capable of transmitting the force and movement information, a force allocation algorithm is implemented herein. A wall facet is divided into three subareas by connecting the vertices p_i to point P_f, with the subscript number of each sub-triangular area A_i is in line with the opposite vertex. Then, the weighting factors w_i of the contact force and stiffness allocation is obtained by dividing the sub-triangular area A_i to the area of its parent facet A, yielding $w_i = \dfrac{A_i}{A}$. The contact force $\boldsymbol{F}$ is then allocated to the vertices composing the contacted facet as defined in Eq. (2).

$$\boldsymbol{F_i} = w_i F \tag{2}$$

As illustrated by Fig. 2, during each cycle of calculations, the DEM model updates vertex positions and contact forces to the FDM model. Simultaneously, the DEM model receives velocities from the FDM model (Hu et al., 2020). This iterative process ensures that forces, velocities, and positions between the two systems are consistently updated and exchanged through this coupling mechanism. For a more detailed description of the wall-zone coupling mechanism, refer to (Zhou et al., 2012; Chen et al., 2021; Itasca Consulting Group, 2022a).

Importantly, to ensure accurate transmission of movement data, a vertex must align precisely with a gridpoint of the zone. To achieve this alignment, the FDM zone entity is generated first, followed by the creation of the coupling wall on the zone's surface to facilitate interactions with particles. In this study, the coupling wall encompasses all surfaces of the geocell.

It is worth noting that unlike the ball entities in DEM, the movement of the wall does not adhere to Newton's laws of motion, and its velocity can be directly assigned. As a consequence, the wall is primarily used to define geometry or loading boundary conditions in DEM models. The primary distinction between a conventional wall and a coupling wall lies in the coupling wall's ability to deform along with the attached zone.

2.2 Contact model and constitutive model

2.2.1 Contact model of discontinuum

In a Discrete Element Method (DEM) model, the relative motion and forces between interconnected grains are governed by a contact model (Asadi et al., 2022). Between any two contacting pieces, only one contact exists (a ball itself constitutes one piece, and the pieces of a wall are referred to as facets). However, a single piece can come into contact with all the pieces surrounding it, meeting the criteria for contact activation. The macroscopic behaviors of the granular assembly, such as deformation and strength, result from the cumulative and integral manifestations of micromechanical interactions among particles (Meng et al., 2023). The selection of an appropriate contact model is essentially a prerequisite for achieving reliable DEM simulations (Wu et al., 2021).

Given the material characteristics (uniform sub-angular sand) and the experimental

conditions (quasi-static drained loading), spherical balls and a linear-based contact model with rolling resistance (RR model) were employed in this study. While using spherical balls provides the best computational efficiency in DEM simulations, it falls short in representing the shape effects of irregular and angular sand particles (Gao and Meguid, 2018a, b; Alabbasi and Hussein, 2021). The inherently rough surface texture of these particles necessitates an increase in rolling resistance (Jiang et al., 2005). Consequently, introducing artificial rolling resistance becomes a rational and effective method for compensating for the limitations of idealized spherical particles (Ai et al., 2011; Wensrich and Katterfeld, 2012).

A local Cartesian coordinate system is automatically established at the contact as illustrated in Fig. 3. This contact plane coordinate system is oriented such that $\vec{n}$ coincides with the contact normal direction while $\vec{s}$ and $\vec{t}$ are orthogonal coordinates on the plane. In addition, the resultant of relative rotation θ_s and θ_t about $\vec{s}$ and $\vec{t}$ is the bending rotation θ_r, and the resultant of relative translation δ_s and δ_t about $\vec{s}$ and $\vec{t}$ is the tangent displacement δ_S.

As illustrated in Fig. 4, rolling resistance linear model gives rise to an elastoplastic behavior. The spring and slider are liable for elastic and plastic deformations, respectively. The divider accounts for the incapability of sustaining any tension force. The shear force and rolling moment cannot infinitely develop with the increase of the tangential translation and rotation, which conform to the Coulomb's friction law (Estrada et al., 2008). There is ultimate shear force F_s^u and torque M_r^u dependent on the magnitude of the normal force that correspondingly limits the development of the shear force and rolling moment. These are

given by Eq. (3) and (4), where F_n is the normal force, and $\bar{R}$ is the effective radius of the contact defined by Eq. (5). Further, the normal stiffness k_n and shear stiffness k_s are mutually independent, whereas the rolling stiffness k_r is dependent on k_s governed by Eq. (6) proposed by Iwashita and Oda (1998).

$$F_s^u = \mu F_n \tag{3}$$

$$M_r^u = \mu_r F_n \bar{R} \tag{4}$$

$$\bar{R} = \frac{R^{(A)} + R^{(B)}}{R^{(A)} R^{(B)}} \tag{5}$$

$$k_r = k_s \bar{R}^2 \tag{6}$$

In summary, the contact force of rolling resistance linear model resolves into three components, normal force F_n, shear force F_s and rolling moment *M*, which are calculated via Eq. (7), (8), and (9), respectively.

$$F_n = k_n \delta_n \tag{7}$$

$$F_s = \begin{cases} k_s \delta_s & F_s \le F_s^u \\ F_s^u & F_s > F_s^u \end{cases} \tag{8}$$

$$M = \begin{cases} k_r \theta_r & M \le M_r^u \\ M_r^u & M > M_r^u \end{cases} \tag{9}$$

In a DEM model, the boundary conditions are primarily defined by the walls composed of manifold triangular facets. The particulate system is confined within these walls. Loadings applied to the system are implemented by adjusting the velocity of the walls. It is important to note that there is no interaction among the walls themselves; they only interact with the particles. A linear contact model without rolling resistance is adopted to describe the contacts between the walls and particles. A notable discrepancy between interparticle interactions and

particle-wall interactions is that the radius of interaction equals the radius of the particle, as walls do not possess a radius property.

In order to achieve a stable equilibrium state characterized by an acceptable number of cycles, a localized damping mechanism was employed. This mechanism is differentiated from a dashpot featuring viscosity, which is typically expressed in relation to the critical-damping ratios for normal and shear modes. The purpose of this localized damping mechanism is to aid in the dissipation of energy within the system. Within this localized damping approach, a constant parameter, denoted as α, is assigned to the contact pieces. The damping force, denoted as F_d, is computed using Eq (10), wherein the subscript *i* represents the degree of freedom spanning from 1 to 6.

$$F_{d(i)} = -\alpha \left| F_i \right| \operatorname{sign}\left(v_i \right) \tag{10}$$

In general, α is set to 0.7 in quasi-static situations (McDowell and Li, 2016).

2.2.2 Constitutive model of continuum

In the realm of continuum mechanics, the stress-strain relationship of a material is established through the employment of a constitutive model (Chen, 2005). The selection of an appropriate constitutive model in FDM is regarded as a cornerstone for accurately defining geocells (Likitlersuang et al., 2018; Sukkarak et al., 2021b). Considering that geocells typically do not exhibit substantial plastic or rupturing deformation even after complete confined compressive loading, the isotropic linear elastic model has been deemed suitable for characterizing geocell behavior in the absence of pronounced failure. This model has been verified and extensively used in modeling geocells (Leshchinsky and Ling, 2013a; Leshchinsky and Ling, 2013b; Hegde and Sitharam, 2015b; Arias et al., 2020), as well as other geosynthetics (Chen et al.,

2021), particularly when there is a lack of notable deformation characteristics, such as plasticity or rupture behavior.

The incremental stress-strain relationship in isotropic linear elastic model is derived based on Hook's law (Itasca Consulting Group, 2022b):

$$\Delta\sigma_{ij} = 2G\Delta\varepsilon_{ij} + \left(K - \frac{2}{3}G\right)\Delta\varepsilon_{kk}\delta_{ij} \tag{11}$$

In this context, $\Delta\sigma_{ij}$ and $\Delta\varepsilon_{ij}$ represent the incremental stress and strain tensors, respectively. G is the shear modulus and K is the bulk modulus of material, which can be related to Young's modulus E and Poisson's ratio v by Eq. (12) (Surarak et al., 2012; Likitlersuang et al., 2013). Consequently, calculating G and K based solely on E and v is sufficient to accurately define the deformation behavior of geocell. This ensures the effective execution of the coupled simulation.

$$\begin{cases} K = \dfrac{E}{3(1-2v)} \\ G = \dfrac{E}{2(1+v)} \end{cases} \tag{12}$$

3 Coupling model of geocell reinforced soils

3.1 Model Configurations

In accordance with the experimental geocell configuration, a hexagonal-shaped geocell was employed. This geocell consisted of one larger-sized cell and three smaller-sized interconnected cells. The objective was to investigate the influence of size factors on the response of geocell-reinforced soils. Additionally, geocell-free soil configurations were established to demonstrate the reinforcement effect. The cross-sectional arrangement of these

systems is illustrated in Fig. 5. For reference purposes, the designations UN, L1, and S3 were utilized to represent the unreinforced soil, the geocell-reinforced soil system with one larger-sized cell, and the system with three smaller-sized interconnected cells, respectively, in the subsequent descriptions.

The geocells were modeled using the Wedge zone, comprising six grid points. The geocell sheet had a thickness of 0.38 mm, consistent with the experiments conducted by Chen et al. (2013). To replicate the L1 and S3 geocells, a total of 44,880 and 63,180 zones were generated, respectively.

Based on the physical dimensions of the soil samples, cylindrical specimens with a diameter of 71.1 mm and a height of 152.4 mm were reproduced, as illustrated in Fig. 6. The geocell height was set at 120.0 mm, centered within the samples, with 16.2 mm margins at the top and bottom, following Chen et al. (2013).

To strike a balance between computational efficiency and adherence to the experimental model, spherical grains with a uniform gradation were generated. Particle sizes were scaled up by a factor of 9, resulting in an acceptable number of particles. Consequently, the particle diameter in the model was increased to 2.25 mm. The dimensional ratio between the smallest extent of the material vessel (71.1 mm) and the largest particle diameter was 31.6. Importantly, as noted by Bathurst and Karpurapu (1993), the scale effect becomes negligible when the dimensional ratio exceeds 6.

3.2 Simulation procedure

In accordance with the laboratory experimental testing procedure, the modeling process was divided into three phases, as illustrated in Fig. 7. The first phase involved the generation of

the soils, geocell, and the material vessel, represented by the balls, zones, and walls, respectively, as shown in Fig. 6. The second phase was responsible for isotropic consolidation, wherein the confinements with three levels of confining pressure (50 kPa, 100 kPa, and 200 kPa) were applied using the servo-mechanism of the wall (Itasca Consulting Group, 2022a). The ultimate phase was controlled by the shearing, the top and bottom synchronously moved downward and upward with a loading rate $H' \times \frac{10^{-6}}{setp}$, where H' is the real-time height of the sample. This rate insures the inertial number I (Lopera Perez et al., 2016; Shire et al., 2021) of the system was smaller than 10^{-3} (e.g., the *I* of UN sample under confining pressure of 100 kPa was approximately 4.5×10^{-5}), which was slow enough to guarantee a quasi-static response. The simulation was terminated when the axial strain was larger than 16%. Noteworthy is that the side cylinder walls still retained the constant confining pressure via the servo-mechanism through the entire loading process.

3.3 Validation of the numerical model

There exists no explicit relationship between the macroscopic properties of materials and the microscopic parameters of contact models. As a result, it becomes essential to determine the microparameters within the Discrete Element Method (DEM) through a calibration procedure that relies on trial and error processes (Villard, 2022). This entails a comparison between the macroscopic behavior resulting from the evolution of microstructural features and the experimental data obtained. The microparameters of the numerical model were continuously adjusted until the macroscopic behaviors closely corresponded with the observed deformability and strength in experiments (Salot et al., 2009; Gao and Meguid, 2022).

In line with the experiments conducted by Chen et al. (2013), a series of triaxial compression tests on both unreinforced and reinforced soils, incorporating geocells in various configurations, were replicated numerically as introduced in section of simulation procedure. The calibrated micromechanical and material parameters for geocell-reinforced soils, as shown in Table 1, successfully captured the macroscopic responses. This success is evident from the strong correlation between the calculated results and the experimental data, illustrated in Fig. 8. Additionally, the coefficient of determination (R^2), a well recognized statistical measure for assessing the goodness-of-fit between numerically simulated and experimentally measured values, was used for evaluation This coefficient, calculated using Eq. (13), compares the experiment data (y) and the computed data (y^*), following Wasserman (2004). An R^2 value closer to 1 indicates a higher degree data correlation. In this study, the average R^2 value was 0.950 across various cases, underscoring the reliability of the model calibration. This high degree of accuracy in the model calibration paves the way for trustworthy analyses in subsequent parts of this study.

$$R^2\left(y, y^*\right) = 1 - \frac{\sum_{i=1}^{n}\left(y_i - y_i^*\right)^2}{\sum_{i=1}^{n}\left(y_i - \bar{y}\right)^2} \qquad R^2 \in [0,\ 1] \tag{13}$$

4 Results and discussion

4.1 Characteristics of the deviator stress curves

The evolution of deviator stress with respect to axial strains plays a crucial role in reflecting the macroscopic mechanical behavior of a soil system from the perspective of shear strength development (Muni, 2010). As illustrated in Fig. 9, the deviator stress for all soil systems exhibited a rapid increase during the initial stage. Subsequently, the increasing trend of

deviator stress at confining pressures of 50 kPa and 100 kPa was sustained until the cessation of compressive loadings for the reinforced soils. In contrast, the deviator stress under the highest confinement, i.e., 200 kPa, gradually reached a steady state at an axial strain of 10%. Beyond the peak, a slight softening trend in deviator stress is observed at all confining pressures for the unreinforced soils, with a more pronounced softening behavior observed at higher levels of confining pressure. In essence, when soils are reinforced, they do not show the same strain softening behavior seen in unreinforced soils. Studies by Rajagopal et al. (1999), Chen et al. (2013), and Haussner et al. (2016) suggest that geocells alter the soil's characteristics, transforming it from brittle to ductile. This change results in the reinforced soils exhibiting improved strength.

4.1.1 Reinforcement efficiency

Under the same reinforcement conditions, the shear strength increases as the confining pressure rises, as depicted in Fig. 10a. The reinforcement effect of S3 was found to be superior to that of L1 at the same level of confining pressure. Chen et al., (2013) introduced the deviator stress ratio ($SR = \frac{(\Delta\sigma_R)_{\max}}{(\Delta\sigma_{UN})_{\max}}$) to evaluate the efficiency of geocell reinforcement under increasing levels of confining pressure. This approach has also been widely employed to assess the reinforcement efficiency of other geosynthetics (Oliaei and Kouzegaran, 2017; Potyondy, 2019). Distinctly inspired by Pires and Palmeira's work in 2021, the coefficient of reinforcement, also known as the efficiency factor, is introduced. This coefficient is defined as the ratio of the difference between reinforced and unreinforced strengths to the unreinforced strength, as expressed in Eq. (14). This approach provides a more

comprehensive assessment of the impact of geocell reinforcement.

$$E_{\Delta\sigma} = \frac{(\Delta\sigma_R)_{\max} - (\Delta\sigma_{UN})_{\max}}{(\Delta\sigma_{UN})_{\max}} \times 100\% \quad (14)$$

Where $(\Delta\sigma_R)_{\max}$ and $(\Delta\sigma_{UN})_{\max}$ are the maximum deviator stress of the reinforced and unreinforced soils, respectively. The calculated $E_{\Delta\sigma}$-value (refer to Fig. 10b) illustrates a decline in the reinforcement efficiency of both L1 and S3 with increasing confining pressure. This correlation aligns closely with the experimental results, thereby further validating the accuracy of the numerical model. Notably, the reinforcement efficiency of S3 consistently surpassed that of L1 under equivalent confining pressures. This suggests that the presence of multiple smaller-sized cells imparts stronger constraints compared to a single larger-sized cell. This observation concurs with the outcomes of prior experimental studies conducted by Pokharel et al. (2010), Hegde and Sitharam (2015), and Dash (2020).

4.1.2 Friction angle and cohesion

Geocell strengthening demonstrates significant cohesive strength enhancement even in cohesionless soils, as indicated by Rajagopal et al. (1999). The strength parameters derived from computational results and Mohr-Coulomb failure envelopes are presented in Table 2, with the numerical data closely aligning with the experimental findings of Chen et al. (2013). It is evident that geocell reinforcement enhances cohesion while minimally impacting the friction angle of the reinforced soils. This observation aligns with earlier research by Bathurst and Karpurapu (1993) as well as Rajagopal et al. (1999).

Furthermore, the apparent cohesion is notably influenced by the size factors of the geocell. An increased number of cells coupled with reduced size effectively mobilizes higher

cohesion, without compromising the internal friction resistance of the soil material. This is attributed to the provision of all-round confinement, enabling the impartation of cohesive strength to the soil.

Considering the disparity in cohesion and friction angle between the reinforced and unreinforced soils, the geocell can be treated as an equivalent material possessing a greater cohesion and the same friction angle as the infilling soil (Vibhoosha et al., 2021). The presence of the geocell provides an extra confining stress onto the confined soil, a value that can be determined using Eq. (15) (Rajagopal et al., 1999).

$$\Delta\sigma_3 = \frac{2C_r}{\sqrt{\frac{1+\sin\varphi}{1-\sin\varphi}}} \tag{15}$$

Observations reveal that S3 induces a higher level of additional confining stress on the confined soil. The pronounced increase in confinement effect noted in S3 can be attributed to the presence of multiple cells. This further substantiates the superior reinforcing performance of S3 compared to L1.

4.2 Geocell deformation characteristics

For the geocell replicated with continuous zones, the deformation of the zone is delineated by the displacement of its constituents, i.e., gridpoints. Due to the confined nature of the geocell-reinforced soils (L1 and S3), which take on the form of a regular prismoid, the displacement field was represented using a cylindrical coordinate system. In each scenario, the origin of the coordinate system (denoted as *O)* was located at the geometric center of the geocell. The *Z* axis was aligned parallel to the direction of axial loading, with positive vertical displacement indicated upwards. Regarding the radial direction, any displacement moving away from the

original point *O* was deemed positive, as depicted in the cylindrical axes in Fig. 11. Radial and vertical displacement contours are depicted in Fig. 11. It is clear that the lateral zones experienced radial displacements in a positive direction. This indicates that the geocell acts like a tensioned hoop, effectively limiting the sideways movement of the soils inside. This alignment concurs with the numerical models' portrayal of shrinkage, coinciding well with experimental observations (refer to Fig. 12c-d).

Vertical displacements in the upper section exhibited negative magnitudes, whereas the lower section displayed positive values. This indicates that the geocells, functioning as a shell column under confined compressive loads, experienced longitudinal shortening while deforming consistently with the granular assembly.

Fig. 12 illustrates the disparity in deformation of the geocell cross-section ($Z = 0$) before and after the application of compression loads. Noteworthy is that the experimentally obtained deformation pattern has also been added in Fig. 12, bearing a similar resemblance to that of numerical observations. In general, both the confined regions of S3 and L1 expanded. However, distinct deformation characteristics are observed, as displayed in Fig. 11a and b. The hexagonal geometry of L1 expanded uniformly, while S3's deformation was primarily concentrated at the outermost perimeters of the cells rather than the shared inner sides. This is evident from the near-zero displacement of the inner sides, which are shared by three interconnected cells. Boundaries located farther from the center exhibited greater displacement than the inner shared sides, highlighting the additional resistance provided by interconnected cells.

Furthermore, stress concentrations led to the wear and tear of all corners of L1 and the corners on the outermost sides of cells in S3 (Hibbeler, 2005).

4.3 Contact network characteristics

Coordination number, denoted as Z, is a fundamental parameter used to characterize the packing structure of granular assemblies. It serves as an indicator of both the connectivity and the intensity of contacts within the assembly (Gao et al., 2020; Liu et al., 2020a). The coordination number is defined as the ratio of the total number of contacts (C_N) to the number of particles (N_p) present (Guo and Zhao, 2013; Cantor et al., 2020).

$$Z = \frac{2C_N}{N_p} \tag{16}$$

Some particles within an assembly are often referred to as "rattlers" or "floaters" due to their having zero or only one contact with neighboring particles. These particles, in fact, do not significantly contribute to the support of external loads and make minimal contributions to the stability of the microstructure. As a result, an alternative definition of coordination number has been introduced, known as the mechanical coordination number, Z^*. This concept, taking into account the presence of floaters, was proposed by (Thornton and Antony, 2000). In this context, N_p^1 represents the number of particles with only one contact, and N_p^0 represents the number of particles with zero contact.

$$Z^* = 2\frac{C_N - N_p^1}{N_p - N_p^1 - N_p^0} \tag{17}$$

Fig. 13 illustrates the evolution of conventional coordination (Z) and mechanical coordination number (Z*) as compressive loadings progress. Initially, Z shows a noticeable increasing trend, followed by a relatively stabilized state before the axial strain reaches 3%.

Similarly, Z* displays a rising tendency during the initial phase, although not as pronounced as Z. Given the constant N_p, the growth of Z can be attributed to the increasing total number of contacts. Conversely, the change in Z* does not exhibit significant growth due to its dependence on the floater particles for the initial compression-induced increase in the total number of contacts. The slight fluctuation in Z* throughout the compression process indicates a relatively stable assembly state with no abrupt changes in the connected grain structure, aligning well with the evolution of deviator stress (refer to Fig. 8).

Evidently, a higher coordination number within an assembly corresponded to increased support or constraints, resulting in a more stable microstructure. Both Z and Z* in reinforced soils exhibited larger values compared to those in unreinforced soils. Additionally, coordination numbers in geocell-reinforced soils with multiple smaller interconnected cells demonstrated larger values when compared to reinforced soils with a single larger-sized geocell. To summarize, geocells with multiple cells exhibited superior reinforcement, supported by the densification of the contact network.

4.4 Stability of the contact

4.4.1 Sliding and rolling contacts

As mentioned earlier, the contact pieces begin to slide or roll continuously only when the shear force or bending moment reaches the limiting values of F_s^u or M_r^u (Bhushan, 2013). This signifies the transition of the stable contact structure into an unsteady state. When a significant portion of contacts becomes unstable, the assembly approaches failure.

The evolution of these four types, characterized by the rolling and sliding states throughout the entire shearing process, is depicted in Fig. 14. The proportions of unstable

contacts in pure sliding (C_s), pure rolling (C_r), and sliding with rolling (C_{sr}) states reached a plateau at a small axial strain of about 3%. Conversely, stable contacts without any occurrence of rolling or sliding (C_{nsr}) decreased due to their complementary relationship with the unstable contacts. This characteristic indicates that the initial compression promptly triggered adjustments to the overall stability of the samples, leading to a quasi-stable state. This quasi-stable state persisted throughout the entire shearing process, preventing abrupt collapse.

Furthermore, the P_{nsr} can be found in an escalating sequence: UN < L1 < S3. In contrast, the unstable contact percentages with regards to rolling (P_r), sliding (P_s), and rolling with sliding (P_{sr}) were in an opposite order. It can be concluded that the existence of geocell reduced the possibility of sliding and rolling occurrences among contacts within the assembly, in particular, S3 gained more competence in abatement of the contact instability. To further analyze the reinforcement efficiency of varied geocell configurations with considerations of size factors, the ratio of P_{nsr} similar to deviator ratio was calculated as $P_{nsr}\ \text{ratio} = \frac{(P_{nsr})_R}{(P_{nsr})_{UN}}$. It can be seen from Fig. 15 that the efficiency of geocell reinforcement declined with the increasing confining pressure from the aspect of sliding-rolling contact states. Therefore, increase in confining pressure weakens the reinforcing effect of geocell on the soils, inferring the reinforcement is less effective subjected to high confinements. This is in a good agreement with experimental results of Chen et al. (2013), which adds more validity to this coupled numerical models.

4.4.2 Redundancy factor

From a structural-mechanical perspective (Kruyt, 2010), a particle possesses six degrees of freedom (DOF): three are linked to translational movement, while the remaining three pertain to rotational mobility. In the case of a contact governed by a linear rolling resistance model, the act of sliding or rolling results in the release of two translational or rotational constraints within the contact plane, respectively (Gong et al., 2012). However, it's worth noting that this contact model does not encompass resistance to twisting (rotation around the normal axis); therefore, a twisting rotation movement remains unconstrained. As a result, our study recognizes that only five degrees of freedom are constrained in total. Further specific details can be found in Table 3.

The ratio of total constraints to the freedom of the particle assembly, defined as the redundancy factor (RF), is utilized in this study to further evaluate the system's stability from the perspective of the sliding-rolling state. This can be calculated using Eq. (18). Here, C_* indicates the number of contacts in the corresponding contact state. Rattler particles, which have zero contacts, are excluded from the total freedom calculation as they do not participate in load support (Kruyt, 2010).

$$RF = \frac{5C_{nsr} + 3C_s + 3C_r + C_{sr}}{6\left(N_p - N_p^0\right)} \tag{18}$$

Throughout the entire process of compression, all variations of the RF remain above 1, indicating an equilibrium solid-like state (Gong et al., 2012; Zhou et al., 2017), as depicted in Fig. 16. A larger *RF* value signifies a higher degree of constraints imposed on the system, consequently leading to greater stabilization of the assembly. Notably, the RF of the

reinforced material surpasses that of the unreinforced material under identical confining pressures. Similarly, the RF trends in S3 consistently outperform those in L1. This observation further supports the notion that adjacent cells in S3 indeed impart additional constraints, effectively confining the soil.

As noted by Gong et al. (2012), the redundancy factor is positively correlated with both coordination number and stable contacts. Interestingly, the evolution of the redundancy factor exhibits a decreasing trend, in contrast to the behavior of coordination numbers (refer to Fig. 13), but is similar to the percentage of C_{nsr} (refer to Fig. 14). This suggests that the impact of losing stable contacts is more significant compared to the effect of gaining additional overall contacts, as indicated by the increase in coordination numbers.

Furthermore, a distinct upward trend is observed following a rapid decline in reinforced soils under a confinement of 50 kPa. Notably, the rising tendency in reinforced soils under a confining pressure of 100 kPa was less pronounced than that under 50 kPa, and the curves for reinforced soils under a confining pressure of 200 kPa remained relatively flat. This trend aligns well with the evolution of deviator stress (see Fig. 9). Consequently, the phenomenon of strain hardening observed in the deviator stress curves against axial strain can be attributed to the micromechanical origins involving the accumulation of the redundancy factor.

4.5 Elastic stiffness tensor

In the realm of DEM, it is firmly established that the elastic behavior of the linear contact model is dictated by two linear springs possessing stiffness values denoted as k_n and k_s in the normal and tangential directions respectively. Consequently, the elastic stiffness matrix

E_{ij}^{c} for a given contact can be defined as shown in Eq. (19), wherein n_i and t_i represent the unit vectors along the normal and shear contact force respectively. Furthermore, the elastic stiffness tensor L_{ijkl} for an assembly is derived under the assumption of uniform strain. This assumption facilitates the assessment of elastic stiffness in a specific loading direction.

$$E_{ij}^{c} = k_n n_i n_j + k_s t_i t_j \tag{19}$$

$$L_{ijkl} = \frac{E_{ik}^{c} b_j b_l}{V} \tag{20}$$

L_{ijkl} is a fourth order isotropic tensor with 81 components, which can be simplified to Eq. (21) because of the symmetrical character, i.e., $L_{ijki} = L_{jikl} = L_{klij}$ (Kruyt, 2010). For conciseness, the evolutions of the elastic stiffness tensor component (see Eq. (21)) only in sample of S3 under the confining pressure of 50 kPa are presented in Fig. 17a.

$$L_{ijkl} = \begin{bmatrix} L_{1111} & L_{1122} & L_{1133} & L_{1112} & L_{1123} & L_{1113} \\ & L_{2222} & L_{2233} & L_{2212} & L_{2223} & L_{2213} \\ & & L_{3333} & L_{3312} & L_{3323} & L_{3313} \\ & & & L_{1212} & L_{1223} & L_{1213} \\ & & & & L_{2323} & L_{2313} \\ Sym. & & & & & L_{1313} \end{bmatrix} \tag{21}$$

The components of L_{ijkl} can be categorized into five groups based on their magnitudes, as depicted in Fig. 17. Group V contains values significantly smaller than those of other groups, approaching zero, thus necessitating no further elaboration. As the soil specimen takes on a cylindrical shape and the radial loadings are uniform, deformations and stresses in directions 1 and 2 remain indistinguishable (here, subscripts 1, 2, and 3 of L_{ijkl} correspond to the x, y, and z axes of the global coordinate system in the models). This explains the near-identical magnitudes of L_{1111} and L_{2222}, as well as L_{1133} and L_{2233}.

The foremost component in Group I is L_{3333}, representing the primary elastic stiffness in the loading direction. At the onset of shearing, the values in the three principal directions (L_{1111}, L_{2222}, L_{3333}) demonstrate close magnitudes, reflecting the isotropic loading state of the soil. With the progression of shearing strength, L_{3333} simultaneously increased, whereas L_{1111} and L_{2222} were on the wane.

The incorporation of geocells plays a predominant role in the evolution of L_{3333} but exerts minimal influence on the other components of the stiffness tensor. This confirms that geocells effectively enhance the infill rigidity in response to compressive loads, aligning well with experimental results obtained by Indraratna et al. (2015). Furthermore, the magnitudes of the elastic stiffness tensor increased as the confining pressure rose.

To elucidate the relationship between the principal components of elastic stiffness (L_{3333}, L_{3333}/L_{rrrr}), and stress (S_{33}, S_{33}/S_{rr}), the parameters and were individually graphed against the parameter in Fig. 18. Here, the subscript *rr* signifies the average elastic stiffness and stress along the 1111 (11) and 2222 (22) directions. Overall, a notable positive linear correlation was observed, with soils under identical confining pressures exhibiting akin slopes (refer to Fig. 18a). Moreover, lower confining pressures were found to yield a steeper slope albeit within a more limited range, as opposed to higher confining pressures.

The stress and stiffness components in the radial direction are illustrated in Fig. 18b. It is noteworthy that all the linear proportions of the curves run in parallel. There are apparent gaps among samples under various reinforcement conditions. Furthermore, the curves for UN, L1, and S3 are clustered from left to right, coinciding well with the strength sequence. The

maximum stiffness ratio for all samples is close to 2.0; however, they exhibit different behaviors after reaching this maximum stiffness ratio. Unreinforced soils experienced a reversal in stiffness ratio, whereas the reinforced soils continued to develop stiffness. This discrepancy can be attributed to the macroscopic deformation associated with strain hardening/softening behavior (Peyneau and Roux, 2008), as depicted in the deviator stress curves (refer to Fig. 9).

For reinforced soils, the final principal stress ratio at low confining pressure exceeded that at high confinement. This observation implies that the presence of geocells significantly extended the upper limit of the principal stress ratio under low confining pressure. This phenomenon explains why the stiffness ratio in soils subjected to high confining pressure was smaller than that in soils subjected to low confinement.

4.6 Contact force and force chain network

A contact force can be decomposed into a normal force and a shear force, as illustrated in Fig. 3. The thresholds of the shear force and rolling torque depend on the magnitude of the normal force. Previous research has confirmed that the primary contributor to the development of deviator stress is the normal contact force (Rothenburg and Bathurst, 1989; Thornton, 2000; Zhao and Zhou, 2017). Therefore, a comprehensive investigation of both the contact force and the force chain network was conducted to better understand the influence of size-related factors on the reinforcing mechanism of geocells. This investigation allows establishing a link between macro-responses and their micro-origins.

4.6.1Force chain network

Fig. 19 depicts the strong force chain network of samples subjected to a confining pressure of

50 kPa upon the completion of compressive loading. The threshold for differentiating between strong and weak contact network has typically been set at the level of the mean contact normal force ($\overline{f}_n$) as suggested by Nie et al. (2021) and Lin et al. (2022). However, in order to better highlight the role of strong contacts in load support, this study adopts a higher threshold, set at twice the mean value, following the approach of Liu et al. (2020a). The front view reveals a concentration of force chains aligned parallel to the axial loading direction. This concentration appears closely linked to the emergence of new column-like load paths, reinforcing the applied stress increment in that specific direction.

Additionally, it is evident that the density and thickness of the contact force chains within the geocell are notably greater compared to those situated along the outer margins of the geocell. To better delineate the effects of geocells in various forms, the mean contact normal force ($\overline{f}_n$) distributed both inside and outside the geocell zone, as well as across the entire soil dimension, was separately calculated and displayed in Fig. 20. Firstly, the magnitude of $\overline{f}_n$ within the entire sample space shared the same sequence as the maximum deviator stress shown in Fig. 10a. This implies that the mean normal force is highly related to the strength of the soils. Secondly, $\overline{f}_n$ from the inside geocell zone was larger than that from the outside. This infers that the inside contacts are the primary source of the strength development owing to the geocell inclusion. For $\overline{f}_n$ inside the geocell zone, S3 exhibited a significantly larger value than L1, while outside showed trivial differences between S3 and L1 (refer to Fig. 20b). This reveals that multiple cells are allowed to bestow more capabilities in mobilizing the confined soils to develop a stronger force chain in response to external loadings.

Chen et al. (2013) concluded that the behavior of geocell-reinforced soil under low confining pressure can be explained by the hoop tension theory, whereas the compression shell theory is better suited to describing the behavior under high confining pressures, as proposed by Henkel and Gilbert (1952). At low confining pressures, the soil is more prone to lateral expansion, and the geocell functions as a hoop, providing additional confining stress to the inner soil. Conversely, under high confining pressures, the lateral displacement of soil particles is reduced, and the geocell behaves like a shell, assisting in supporting compressive loads. As a result, the ratio between the inside and outside of $\overline{f}_n$ decreases as the confining pressure increases (refer to Fig. 20c). This observation further validates the hoop-shell theory at the microscopic level.

Moreover, the evolution of the inside/outside $\overline{f}_n$ ratio in Fig. 20c closely resembles the increasing rate of deviator stress (as shown in Fig. 10b). This similarity suggests that the efficiency of reinforcement diminishes at high confining pressures due to reduced lateral deformation of the soil mass. Consequently, the hoop confining effect cannot be fully realized. Additionally, at significant levels of confinement, the vertical performance of the geocell is insufficient when compared to its lateral behavior. This weakness is exemplified by the ratio approaching 1 under a confining pressure of 200 kPa.

Conversely, force chains within the unreinforced soils exhibit a uniform distribution across all vessel dimensions. This observation supports the notion that the geocell effectively mobilized the soil to establish a quasi-rigid composite, thereby enhancing the load-carrying capacity while mitigating lateral spreading of the infilled soils. To summarize, the

confinement effect exerted by the geocell positively influences soil stability, and the confinement effect abates as the confining pressure increasing, as manifested by the microscopic characteristics of the concentrated force chains within the geocell structure.

4.6.2 3D histogram

To understand the impact of geocell size-related factors on the spatial distribution of normal contact forces within the soil assembly, spherical histograms were employed herein. Normal contact force f_n is a vector quantity that, in a Cartesian coordinate system, can be described using component form as $\left(f_{nx},\ f_{ny},\ f_{nz}\right)$.The force f_n can also be mapped into the spherical coordinate system as outlined in Eq. (22). In this equation, F_{mag} is the magnitude of the f_n, ϕ and θ represents the polar angle and azimuthal angle depict the orientation of f_n in the space (refer to Fig. 21) . In this approach, the orientation sphere was divided into 600 subregions using 40 latitude lines and 15 meridians, ensuring equal areas for each subregion (He et al., 2022). All contacts were mapped into the spherical coordinate system then grouped according to the orientation $\left(\phi,\ \theta\right)$ into the subregions. In spherical histogram, each subdivision was represented by a bar. The length and color intensity of the bar reflects the normalized local average of the normal contact force ($\overline{F}_{magi} / \overline{F}_{mag0}$). Here, $\overline{F}_{magi}$ represents the mean magnitude of normal contact forces within a specific subregion. $\overline{F}_{mag0}$ signifies the average of these magnitudes across all subregions (Ouadfel and Rothenburg, 2001).

$$\begin{cases} F_{mag} = \sqrt{f_{nx}^2 + f_{ny}^2 + f_{nz}^2} \\ \phi = Arctan\left(\sqrt{f_{nx}^2 + f_{ny}^2},\ f_{nz}\right) \\ \theta = Arctan\left(f_{ny},\ f_{nz}\right) \end{cases} \tag{22}$$

In the ideal scenario of perfectly isotropic distribution of normal contact forces, the 3D histogram's shape would resemble a unit sphere with a radius of 1. Deviations in the histogram outline from this spherical shape indicate the anisotropic nature of the particle assembly (Zhao and Zhou, 2017).

Initially, during compression, the 3D histograms of all samples, whether reinforced or not, approximated a sphere with a unit radius (see Fig. 22a, b, c). This suggests that all samples were uniformly compacted initially, exhibiting a well-isotropic stress state. The standard deviation (SD) is applied to quantitatively evaluate the uniformity of the contact normal force. The low standard deviation at the initial state reflects the uniform contact distribution. However, as the compression proceeds, the distribution of the 3D histogram elongated, taking on the shape of an upright peanut (Fig. 22d, f). The high SD unveils a relatively an anisotropic contact distribution. This elongation implies an increased number of contacts and force magnitude along the loading axis compared to other directions, highlighting a high degree of shear induced anisotropy. Moreover, the orientation distribution of strong contact normal forces is primarily concentrated at the top and bottom regions. These regions align with the Z axis in the Cartesian coordinate system, suggesting a directionality of these forces. This alignment is consistent with the principal orientation of the force chain network shown in Fig. 19, indicating a predominant force transfer towards the compressive loading axis (Zhou et al., 2015).

In conclusion, not only did the number of contacts increase along the loading axis, but the magnitude of normal contact forces also grew. Additionally, the histogram of unreinforced

soil (Fig. 22d) displayed a narrower spread along the horizontal direction than geocell-reinforced soils S3 (Fig. 22e) and L1 (Fig. 22f) suggesting a relatively more anisotropic behavior. Clearly, the standard deviation for UN exceeds that of S3 and L1. This finding is consistent with the significantly greater shear deformation observed in unreinforced soils, as compared to geocell-reinforced soils S3 (Fig. 22e) and L1 (Fig. 22f). This further confirms that the inclusion of a geocell promoted a more uniform and homogenous distribution of contact forces. The use of geocell increases the number of contacts that are oriented horizontally. This leads to a higher number of contact forces with a greater magnitude, which are more horizontally inclined compared to those in unreinforced soil. Importantly, the histogram of geocell-reinforced soil with a single larger-sized cell exhibited a relatively more uniform distribution. This could be attributed to the increased confinement effect facilitated by multiple cells in the geocell, leading to the mobilization of a larger volume of soil in response to enhanced confinement.

5 Limitation of the study

This study employs a coupled FDM-DEM numerical simulation, effectively harnessing the intrinsic properties of soil and geocell to mirror real-world conditions. Despite its advanced three-dimensional approach, the research is based solely on a laboratory model. It focuses on how different sizes of geocells affect the stress-strain responses in geocell-reinforced granular soil. The study sheds light on the microscopic mechanisms that influence the macro-mechanical behavior of these soils, with a special focus on the impact of geocell size. However, the study's findings are derived from small-scale model tests. To validate these

results, future research should include large-scale experimental or field tests. Such tests in actual field conditions will deepen our understanding of how geocell size factors into the reinforcement process. This knowledge will be crucial for developing guidelines for the design and construction of geocell-reinforced soil systems.

6 Conclusions

In this study, a coupled three-dimensional continuum-discontinuum framework was established to analyze the influence of cell size and quantity on the confining mechanisms of geocell-reinforced soils. The geocell was simulated using continuum elements within the Finite Difference Method (FDM), while the backfill material was replicated using discontinuum entities within the Discrete Element Method (DEM), tailored to their inherent characteristics. Through comprehensive investigations into the impact of size-related factors on the macroscopic behavior of geocell-reinforced soils, along with the micromechanical origins in response to confined compressions, we derived the following novel findings:

1. The reinforcement mechanism of the geocell primarily arises from its confinement effect, leading to increased infill rigidity and enhanced load-carrying capacity. This observation is supported by micromechanical evidence such as the densification of interparticle contacts, reduction in the number of less-contributing floating particles, homogenization of contact network magnitudes and orientations, prevention of strong force chain buckling and rupture, and enhancement of the principal component of the elastic stiffness tensor (L_{3333}) as rigidity increases due to the mobilization of infill soils, resulting in a quasi-rigid composite.

2. Enhanced confinement provided by geocells helps prevent lateral spreading of granular soil. Moreover, geocell reinforcement with multiple cells demonstrates superior performance compared to single large-sized cell configurations. This enhancement is attributed to the additional constraints imposed by adjacent cells, effectively curbing lateral expansion and constraining the mobilization of infill soils and geocells in multi-cell setups.
3. As confining pressure on reinforced soil increases, the reinforcing effect becomes less pronounced. This phenomenon can be attributed to microscopic origins where heightened confinement reduces the percentage of unstable contacts and limits geocell deformation, thereby hindering its ability to mobilize soil into a geocell-soil composite as confinement levels rise. As the confining pressure increase, the decline in reinforcement efficiency is associated with the constrained lateral deformation of the soil assembly. Additionally, the function of the geocell in the soil shifts from being tensioned hoops to compressed shells. While geocells excel at sustaining lateral tension, they exhibit a limited capability to support vertical compression. Consequently, the reinforcing effect of geocells under high confining pressure is less pronounced compared to that under low confining pressure. This observation is substantiated by the ratio between the mean normal force within the geocell zone and that outside it.

The results from this study can be useful in the design and construction of geocell reinforced soils. This study provide encouragement for the application of geocell reinforcement with

multiple cells. In addition, utilization of geocells in low confinement is also recommended.

Data availability statement

Data generated or analyzed during this study are available from the corresponding author upon reasonable request

Acknowledgement

Financial support provided by the National Natural Science Foundation of China under Grant No. 42107192 and the Shanghai Sailing Program (21YF1419200). The numerical software utilized in this research is made possible by funding from McGill University.

Competing interests

The authors declare there are no competing interests.

References

Ai, J., Chen, J.-F., Rotter, J.M., Ooi, J.Y., 2011. Assessment of rolling resistance models in discrete element simulations. Powder Technology 206, 269-282.

Alabbasi, Y., Hussein, M., 2021. Geomechanical Modelling of Railroad Ballast: A Review. Archives of Computational Methods in Engineering 28, 815-839.

Amiri, A., Moghaddas Tafreshi, S.N., Dawson, A.R., 2023. Vibration response of machine foundations protected by use of adjacent multi-layer geocells. Geotextiles and Geomembranes 51, 15-35.

Ari, A., Misir, G., 2021. Three-dimensional numerical analysis of geocell reinforced shell foundations. Geotextiles and Geomembranes 49, 963-975.

Arias, J.L., Inti, S., Tandon, V., 2020. Influence of Geocell Reinforcement on Bearing Capacity of Low-Volume Roads. Transportation in Developing Economies 6, 5.

Asadi, M., Mahboubi, A., Thoeni, K., 2022. Towards more realistic modelling of sand–rubber

mixtures considering shape, deformability, and micro-mechanics. Canadian Geotechnical Journal 60, 182-197.

Bathurst, R., Karpurapu, R., 1993. Large-Scale Triaxial Compression Testing of Geocell-Reinforced Granular Soils. Geotechnical Testing Journal 16, 296-303.

Bergado, D.T., Jamsawang, P., Jongpradist, P., Likitlersuang, S., Pantaeng, C., Kovittayanun, N., Baez, F., 2022. Case study and numerical simulation of PVD improved soft Bangkok clay with surcharge and vacuum preloading using a modified air-water separation system. Geotextiles and Geomembranes 50, 137-153.

Bhushan, B., 2013. Principles and applications of tribology, Second edition.. ed. Chichester, West Sussex, UK : Wiley.

Biabani, M.M., Indraratna, B., Ngo, N.T., 2016. Modelling of geocell-reinforced subballast subjected to cyclic loading. Geotextiles and Geomembranes 44, 489-503.

Biswas, A., Krishna, A.M., 2017. Geocell-Reinforced Foundation Systems: A Critical Review. International Journal of Geosynthetics and Ground Engineering 3, 17.

Cambou, B., Dubujet, P., Nouguier-Lehon, C., 2004. Anisotropy in granular materials at different scales. Mechanics of Materials 36, 1185-1194.

Cantor, D., Azéma, E., Preechawuttipong, I., 2020. Microstructural analysis of sheared polydisperse polyhedral grains. Physical Review E 101, 062901.

Chen, H., 2005. Constitutive equations for concrete and soil China Architecture & Building Press, Beijing.

Chen, R.-H., Huang, Y.-W., Huang, F.-C., 2013. Confinement effect of geocells on sand samples under triaxial compression. Geotextiles and Geomembranes 37, 35-44.

Chen, W.-B., Xu, T., Zhou, W.-H., 2021. Microanalysis of smooth Geomembrane–Sand interface using FDM–DEM coupling simulation. Geotextiles and Geomembranes 49, 276-288.

Christoffersen, J., Mehrabadi, M.M., Nemat-Nasser, S.J.J.o.A.M., 1981. A Micromechanical Description of Granular Material Behavior. 48, 339.

Cundall, P.A., Strack, O.D.L., 1979. A discrete numerical model for granular assemblies.

Géotechnique 29, 47-65.

Dash, S.K., 2020. Effect of Geocells Geometry on the Performance of the Foundations, in: Sitharam, T.G., Hegde, A.M., Kolathayar, S. (Eds.), Geocells: Advances and Applications. Springer Singapore, Singapore, pp. 131-152.

Emersleben, A., Meyer, N., 2009. Interaction Between Hoop Stresses and Passive Earth Resistance in Single and Multiple Geocell Structures, 1st African Regional Conference, GEO Afirca, Cape Town.

Estrada, N., Taboada, A., Radjai, F., 2008. Shear strength and force transmission in granular media with rolling resistance. 78, 021301.

Gao, G., Meguid, M.A., 2018a. Effect of particle shape on the response of geogrid-reinforced systems: Insights from 3D discrete element analysis. Geotextiles and Geomembranes 46, 685-698.

Gao, G., Meguid, M.A., 2018b. On the role of sphericity of falling rock clusters—insights from experimental and numerical investigations. Landslides 15, 219-232.

Gao, G., Meguid, M.A., 2022. Microscale Characterization of Fracture Growth in Increasingly Jointed Rock Samples. Rock Mechanics and Rock Engineering 55, 6033-6061.

Gao, G., Meguid, M.A., Chouinard, L.E., 2020. On the role of pre-existing discontinuities on the micromechanical behavior of confined rock samples: a numerical study. Acta Geotechnica 15, 3483-3510.

Gedela, R., Karpurapu, R., 2021. Influence of pocket shape on numerical response of geocell reinforced foundation systems. 28, 327-337.

Gong, G., Lin, P., Qin, Y., Wei, J., 2012. Dem simulation of liquefaction for granular media under undrained axisymmetric compression and plane strain conditions. Acta Mechanica Solida Sinica 25, 562-570.

Grange, S.p.e., Salciarini, D.e., 2022. Deterministic numerical modeling of soil-structure interaction. London, UK : ISTE, Ltd. Hoboken, NJ : Wiley

Guo, N., Zhao, J., 2013. The signature of shear-induced anisotropy in granular media.

Computers and Geotechnics 47, 1-15.

Haussner, C., Kiyota, T., Xu, Z., 2016. Effect of spacing of transverse members on pulloutresistance of a square-shaped geocell embedded in sandy and gravelly backfill materials. Japanese Geotechnical Society Special Publication 4, 109-114.

He, G., Karatza, Z., Papanicolopulos, S.-A., 2022. Contact orientation distributions for visualisation of granular fabric. Granular Matter 24, 44.

Hegde, A., 2017. Geocell reinforced foundation beds-past findings, present trends and future prospects: A state-of-the-art review. Construction and Building Materials 154, 658-674.

Hegde, A., Sitharam, T.G., 2015a. 3-Dimensional numerical modelling of geocell reinforced sand beds. Geotextiles and Geomembranes 43, 171-181.

Hegde, A.M., Sitharam, T.G., 2015b. Three-dimensional numerical analysis of geocell-reinforced soft clay beds by considering the actual geometry of geocell pockets. Canadian Geotechnical Journal 52, 1396-1407.

Henkel, D.J., Gilbert, G.D., 1952. The Effect Measured of the Rubber Membrane on the Triaxial Compression Strength of Clay Samples. Géotechnique 3, 20-29.

Hibbeler, R.C., 2005. Mechanics of materials, 6th ed.. ed. Upper Saddle River, N.J. : Pearson/Prentice Hall, Upper Saddle River, N.J.

Hu, W.R., Liu, K., Potyondy, D.O., Zhang, Q.B., 2020. 3D continuum-discrete coupled modelling of triaxial Hopkinson bar tests on rock under multiaxial static-dynamic loads. International Journal of Rock Mechanics and Mining Sciences 134, 104448.

Huang, M., Lin, C., Pokharel, S.K., 2023. Freeze-thaw behavior of geocell-reinforced bases considering different fines contents. Geosynthetics International 0, 1-18.

Indraratna, B., Biabani, M.M., Nimbalkar, S., 2015. Behavior of Geocell-Reinforced Subballast Subjected to Cyclic Loading in Plane-Strain Condition. Journal of Geotechnical and Geoenvironmental Engineering 141, 04014081.

Itasca Consulting Group, I., 2022a. PFC 6.0 Documentation.

Itasca Consulting Group, I., 2022b. FLAC3D 6.0 Documentation.

Iwashita, K., Oda, M., 1998. Rolling Resistance at Contacts in Simulation of Shear Band

Development by DEM. Journal of Engineering Mechanics-asce - J ENG MECH-ASCE 124.

Jiang, M.J., Yu, H.S., Harris, D., 2005. A novel discrete model for granular material incorporating rolling resistance. Computers and Geotechnics 32, 340-357.

Jirawattanasomkul, T., Kongwang, N., Jongvivatsakul, P., Likitlersuang, S., 2018. Finite element modelling of flexural behaviour of geosynthetic cementitious composite mat (GCCM). Composites Part B: Engineering 154, 33-42.

Jirawattanasomkul, T., Kongwang, N., Jongvivatsakul, P., Likitlersuang, S., 2019. Finite element analysis of tensile and puncture behaviours of geosynthetic cementitious composite mat (GCCM). Composites Part B: Engineering 165, 702-711.

Kruyt, N.P., 2010. Micromechanical study of plasticity of granular materials. Comptes Rendus Mécanique 338, 596-603.

Leshchinsky, B., Ling, H., 2013a. Effects of Geocell Confinement on Strength and Deformation Behavior of Gravel. Journal of Geotechnical and Geoenvironmental Engineering 139, 340-352.

Leshchinsky, B., Ling, H.I., 2013b. Numerical modeling of behavior of railway ballasted structure with geocell confinement. Geotextiles and Geomembranes 36, 33-43.

Likitlersuang, S., Chheng, C., Surarak, C., Balasubramaniam, A., 2018. Strength and Stiffness Parameters of Bangkok Clays for Finite Element Analysis. Geotechnical Engineering Journal of the SEAGS & AGSSEA 49.

Likitlersuang, S., Teachavorasinskun, S., Surarak, C., Oh, E., Balasubramaniam, A., 2013. Small strain stiffness and stiffness degradation curve of Bangkok Clays. Soils and Foundations 53, 498-509.

Lin, M., Zhou, W., Liu, J., Ma, G., Cao, X., 2022. A topological view on microscopic structural evolution for granular material under loading and unloading path. Computers and Geotechnics 141, 104530.

Liu, J., Zhou, W., Ma, G., Yang, S., Chang, X., 2020a. Strong contacts, connectivity and fabric anisotropy in granular materials: A 3D perspective. Powder Technology 366, 747-

760.

Liu, Y., Deng, A., Jaksa, M., 2018. Three-dimensional modeling of geocell-reinforced straight and curved ballast embankments. Computers and Geotechnics 102, 53-65.

Liu, Y., Deng, A., Jaksa, M., 2020b. Three-Dimensional Discrete-Element Modeling of Geocell-Reinforced Ballast Considering Breakage. International Journal of Geomechanics 20, 04020032.

Lopera Perez, J.C., Kwok, C.Y., O'Sullivan, C., Huang, X., Hanley, K.J., 2016. Assessing the quasi-static conditions for shearing in granular media within the critical state soil mechanics framework. Soils and Foundations 56, 152-159.

Mahgoub, A., El Naggar, H., 2020. Coupled TDA–Geocell Stress-Bridging System for Buried Corrugated Metal Pipes. Journal of Geotechnical and Geoenvironmental Engineering 146, 04020052.

McDowell, G.R., Li, H., 2016. Discrete element modelling of scaled railway ballast under triaxial conditions. Granular Matter 18, 66.

Meng, Q., Xue, H., Song, H., Zhuang, X., Rabczuk, T., 2023. Rigid-Block DEM Modeling of Mesoscale Fracture Behavior of Concrete with Random Aggregates. Journal of Engineering Mechanics 149, 04022114.

Muni, B., 2010. Soil mechanics and foundations, 3rd ed. JOHN WILEY & SONS, INC.

Nayyar, A.S., Sahu, A.K., 2021. Numerical analysis of railway substructure with geocell-reinforced ballast. Geomechanics and Geoengineering, 1-11.

Ngo Ngoc, T., Indraratna, B., Rujikiatkamjorn, C., Mahdi Biabani, M., 2016. Experimental and Discrete Element Modeling of Geocell-Stabilized Subballast Subjected to Cyclic Loading. Journal of Geotechnical and Geoenvironmental Engineering 142, 04015100.

Ngo, T.P., Likitlersuang, S., Takahashi, A., 2019. Performance of a geosynthetic cementitious composite mat for stabilising sandy slopes. Geosynthetic International 26, 309-319.

Nie, J.-Y., Cao, Z.-J., Li, D.-Q., Cui, Y.-F., 2021. 3D DEM insights into the effect of particle overall regularity on macro and micro mechanical behaviours of dense sands. Computers and Geotechnics 132, 103965.

O'Sullivan, C.a., 2014. Particulate Discrete Element Modelling : A Geomechanics Perspective, First edition.. ed. Boca Raton, FL : CRC Press.

Oliaei, M., Kouzegaran, S., 2017. Efficiency of cellular geosynthetics for foundation reinforcement. Geotextiles and Geomembranes 45, 11-22.

Ouadfel, H., Rothenburg, L., 2001. `Stress–force–fabric' relationship for assemblies of ellipsoids. Mechanics of Materials 33, 201-221.

Peyneau, P.-E., Roux, J.-N., 2008. Solidlike behavior and anisotropy in rigid frictionless bead assemblies. Physical Review E 78, 041307.

Pires, A.C.G., Palmeira, E.M., 2021. The influence of geosynthetic reinforcement on the mechanical behaviour of soil-pipe systems. Geotextiles and Geomembranes 49, 1117-1128.

Pokharel, S.K., Han, J., Leshchinsky, D., Parsons, R.L., Halahmi, I., 2010. Investigation of factors influencing behavior of single geocell-reinforced bases under static loading. Geotextiles and Geomembranes 28, 570-578.

Potyondy, D., 2019. Pavement-Design Package for PFC3D. Itasca Consulting Group, Inc., Minneapolis, Minnesota.

Rajagopal, K., Krishnaswamy, N.R., Madhavi Latha, G., 1999. Behaviour of sand confined with single and multiple geocells. Geotextiles and Geomembranes 17, 171-184.

Rothenburg, L., Bathurst, R.J., 1989. Analytical study of induced anisotropy in idealized granular materials. Géotechnique 39, 601-614.

Saint-Cyr, B., Delenne, J.Y., Voivret, C., Radjai, F., Sornay, P., 2011. Rheology of granular materials composed of nonconvex particles. Physical Review E 84, 041302.

Salot, C., Gotteland, P., Villard, P., 2009. Influence of relative density on granular materials behavior: DEM simulations of triaxial tests. Granular Matter 11, 221-236.

Satyal, S.R., Leshchinsky, B., Han, J., Neupane, M., 2018. Use of cellular confinement for improved railway performance on soft subgrades. Geotextiles and Geomembranes 46, 190-205.

Sawada, Y., Kitada, M., Ling, H.I., Kawabata, T., 2023. Lateral force–displacement

relationships for shallowly buried pipe reinforced by geocells. Geosynthetics International 0, 1-14.

Sheikh, I.R., Mandhaniya, P., Shah, M.Y., 2021. A Parametric Study on Pavement with Geocell Reinforced Rock Quarry Waste Base on Dredged Soil Subgrade. International Journal of Geosynthetics and Ground Engineering 7, 32.

Sheikh, I.R., Shah, M.Y., 2021. State-of-the-Art Review on the Role of Geocells in Soil Reinforcement. Geotechnical and Geological Engineering 39, 1727-1741.

Shire, T., Hanley, K.J., Stratford, K., 2021. DEM simulations of polydisperse media: efficient contact detection applied to investigate the quasi-static limit. Computational Particle Mechanics 8, 653-663.

Sitharam, T.G.e., Hegde, A.M.e., Kolathayar, S.e., SpringerLink, 2020. Geocells Advances and Applications, 1st ed. 2020.. ed. Singapore : Springer Singapore : Imprint: Springer.

Sukkarak, R., Jongpradist, P., Kongkitkul, W., Jamsawang, P., Likitlersuang, S., 2021a. Investigation on load-carrying capacity of geogrid-encased deep cement mixing piles. Geosynthetics International 28, 450-463.

Sukkarak, R., Likitlersuang, S., Jongpradist, P., Jamsawang, P., 2021b. Strength and stiffness parameters for hardening soil model of rockfill materials. Soils and Foundations 61, 1597-1614.

Surarak, C., Likitlersuang, S., Wanatowski, D., Balasubramaniam, A., Oh, E., Guan, H., 2012. Stiffness and strength parameters for hardening soil model of soft and stiff Bangkok clays. Soils and Foundations 52, 682-697.

Thornton, C., 2000. Numerical simulations of deviatoric shear deformation of granular media. Géotechnique 50, 43-53.

Thornton, C., Antony, S.J., 2000. Quasi-static shear deformation of a soft particle system. Powder Technology 109, 179-191.

Tran, V.D.H., Meguid, M.A., Chouinard, L.E., 2013. A finite–discrete element framework for the 3D modeling of geogrid–soil interaction under pullout loading conditions. Geotextiles and Geomembranes 37, 1-9.

Tran, V.D.H., Meguid, M.A., Chouinard, L.E., 2015. Three-Dimensional Analysis of Geogrid-Reinforced Soil Using a Finite-Discrete Element Framework. International Journal of Geomechanics 15, 04014066.

Vibhoosha, M.P., Bhasi, A., Nayak, S., 2021. A Review on the Design, Applications and Numerical Modeling of Geocell Reinforced Soil. Geotechnical and Geological Engineering 39, 4035-4057.

Villard, P., 2022. DEM Approach of the Modeling for Geotechnical Structures in Interaction with Reinforcements, Deterministic Numerical Modeling of Soil–Structure Interaction, pp. 55-99.

Wasserman, L.a., 2004. All of Statistics A Concise Course in Statistical Inference. New York, NY : Springer New York : Imprint: Springer.

Wensrich, C.M., Katterfeld, A., 2012. Rolling friction as a technique for modelling particle shape in DEM. Powder Technology 217, 409-417.

Wu, M., Wang, J., Zhao, B., 2021. DEM modeling of one-dimensional compression of sands incorporating statistical particle fragmentation scheme. Canadian Geotechnical Journal 59, 144-157.

Xu, C., 2021. Geosynthetics. China Architecture & Building Press, Beijing.

Zhao, S., Evans, T.M., Zhou, X., 2018. Effects of curvature-related DEM contact model on the macro- and micro-mechanical behaviours of granular soils. 68, 1085-1098.

Zhao, S., Evans, T.M., Zhou, X., Zhou, S., 2016. Discrete element method investigation on thermally-induced shakedown of granular materials. Granular Matter 19, 11.

Zhao, S., Zhou, X., 2017. Effects of particle asphericity on the macro- and micro-mechanical behaviors of granular assemblies. Granular Matter 19, 38.

Zhao, Y., Lu, Z., Liu, J., Yao, H., Tang, C., Nie, Y., Zhang, J., 2023. Creep behavior and viscoelastic-plastic models for polymer-blend HDPE geocell sheets based on the stepped isothermal method. Geotextiles and Geomembranes.

Zhou, J., Jian, Q.-w., Zhang, J., Guo, J.-j., 2012. Coupled 3D discrete-continuum numerical modeling of pile penetration in sand. Journal of Zhejiang University SCIENCE A 13,

44-55.

Zhou, W., Liu, J., Ma, G., Chang, X., 2017. Three-dimensional DEM investigation of critical state and dilatancy behaviors of granular materials. Acta Geotechnica 12, 527-540.

Zhou, W., Yang, L., Ma, G., Chang, X., Cheng, Y., Li, D., 2015. Macro–micro responses of crushable granular materials in simulated true triaxial tests. Granular Matter 17, 497-509.

Figure captions

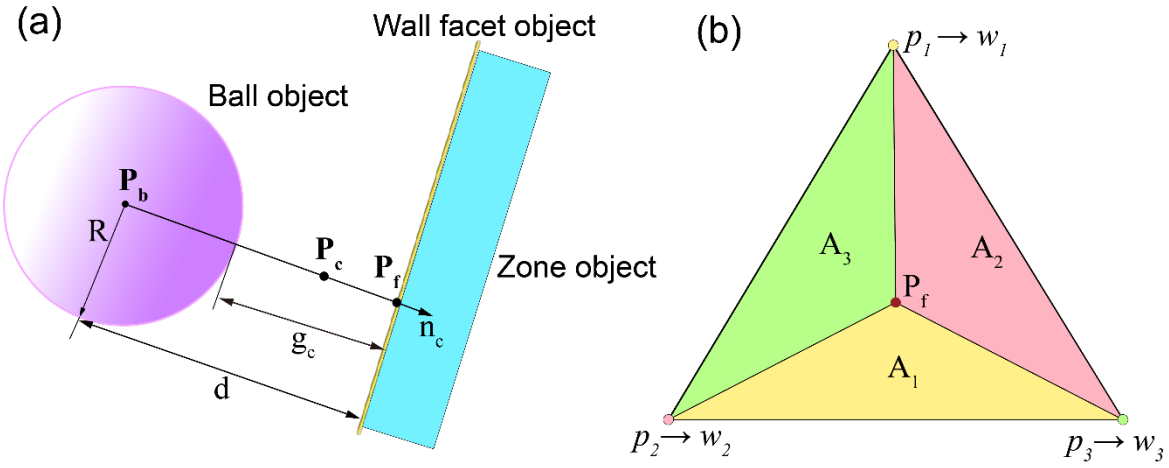

Fig. 1 (a) Contact interface between ball-facet; (b) Barycentric interpolation scheme of a facet

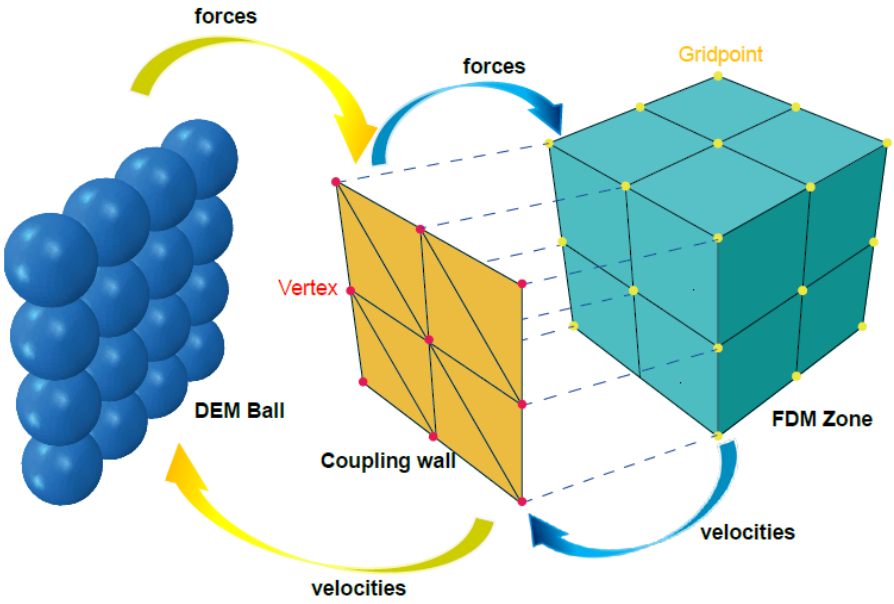

Fig. 2 Coupling mechanism of the FDM-DEM objects

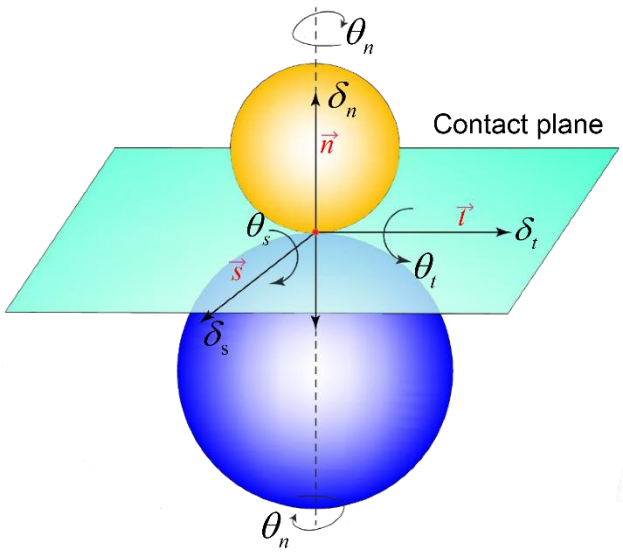

Fig. 3 The local contact coordinate system and relative movements between two particles

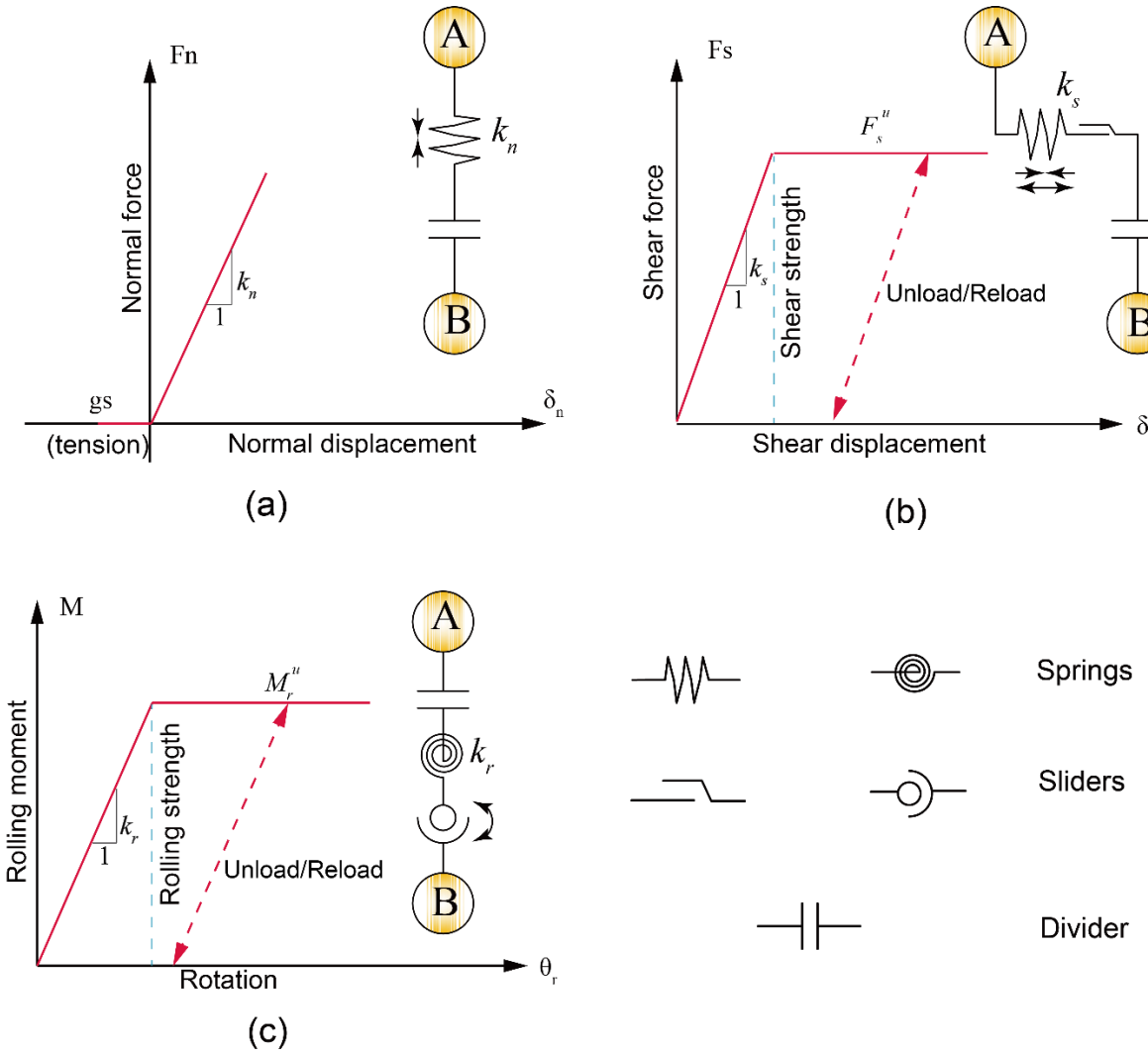

Fig. 4 Behavior and rheological components of the RR model: (a) normal translation; (b) tangent translation; (c) bending rotation

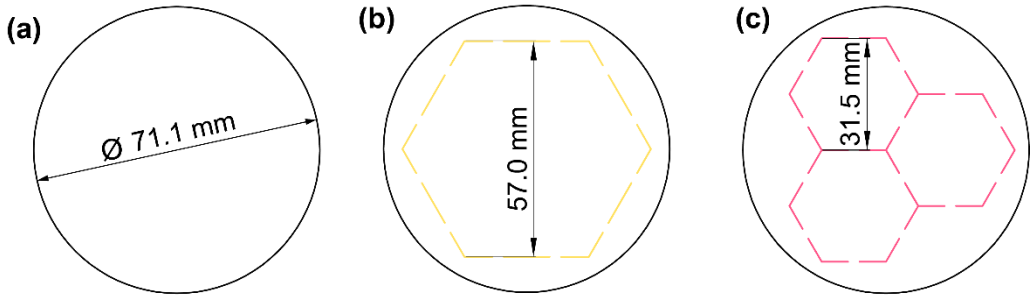

Fig. 5 Cross-section of the samples: a) UN; b) L1; c) S3

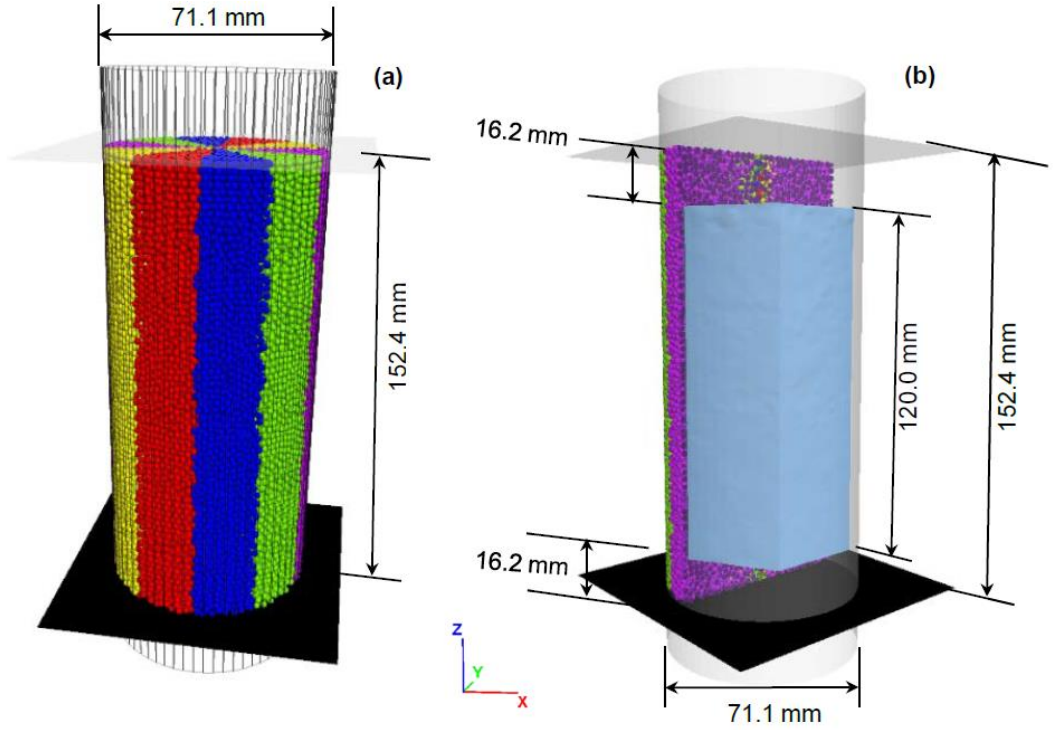

Fig. 6 Dimensions of the triaxial compression sample

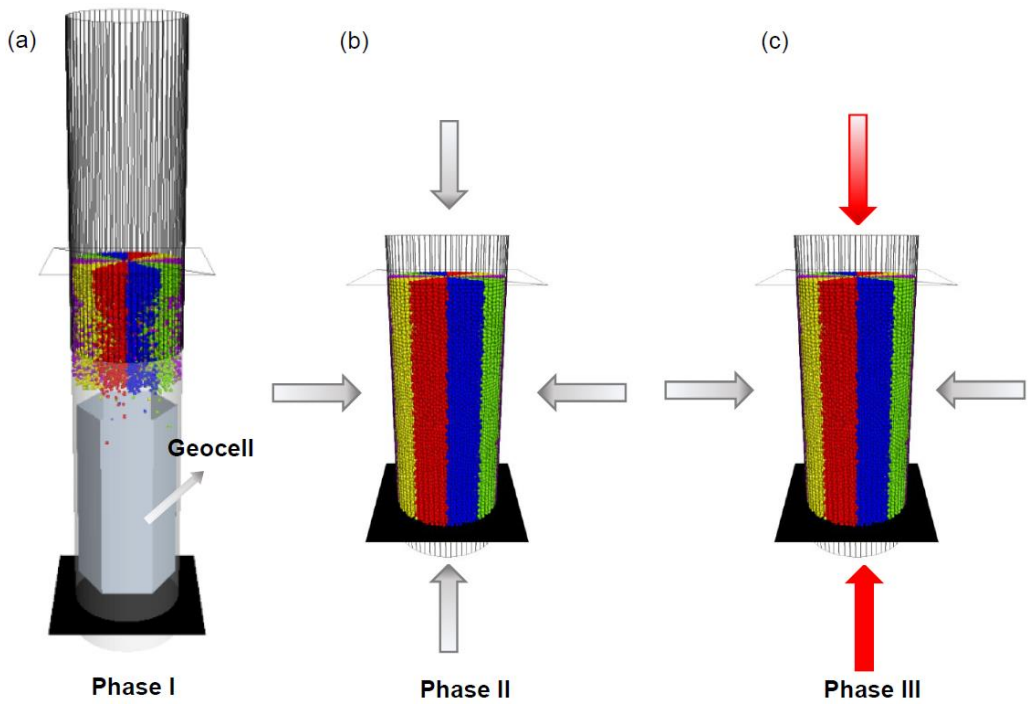

Fig. 7 Three stages of a triaxial compression test simulation: (a) phase I; (b) phase II; (c) phase III

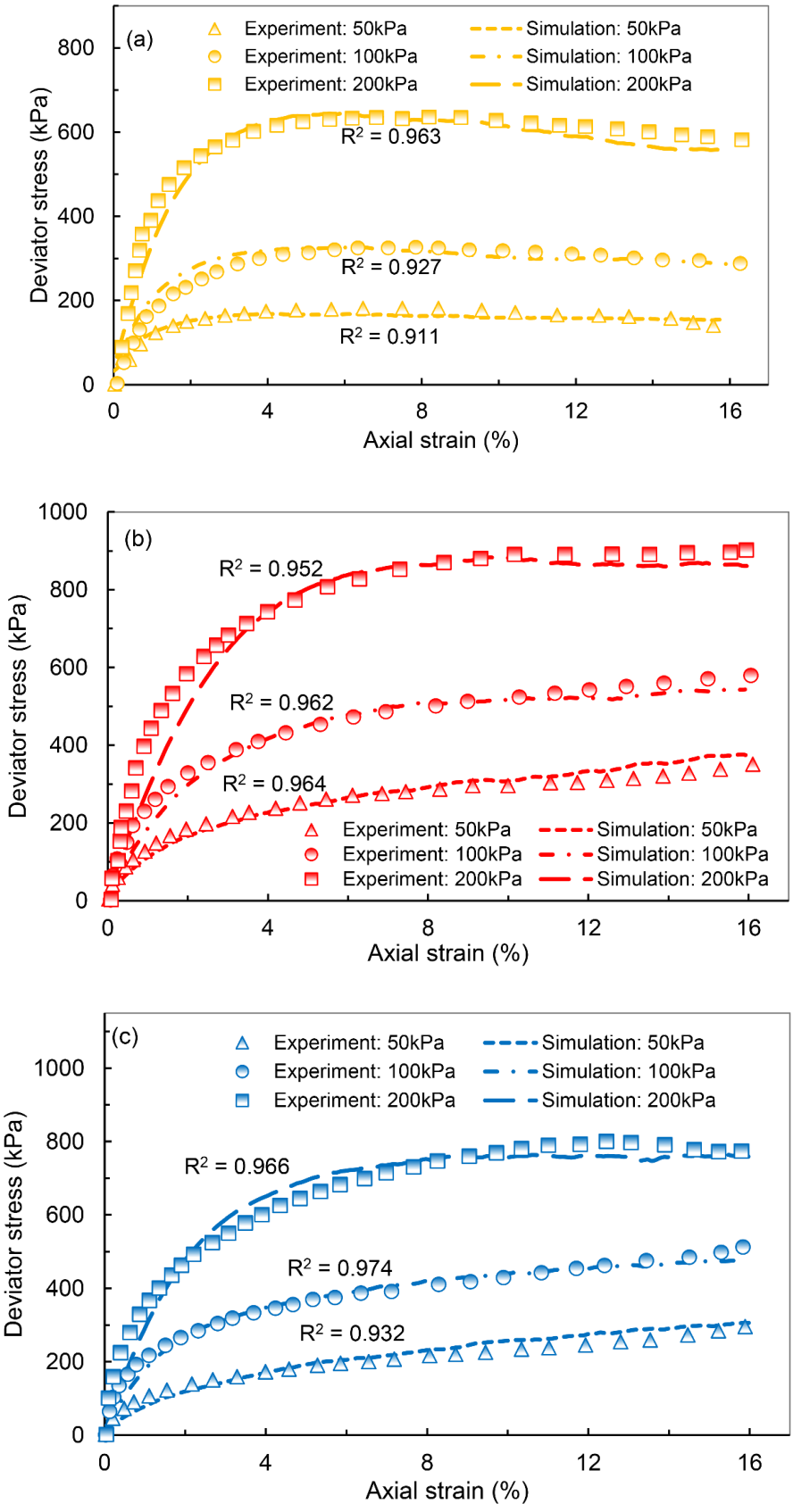

Fig. 8 Comparisons of deviator stress versus axial strain obtained from the simulations and experiments: (a) UN; (b) S3; (c) L1

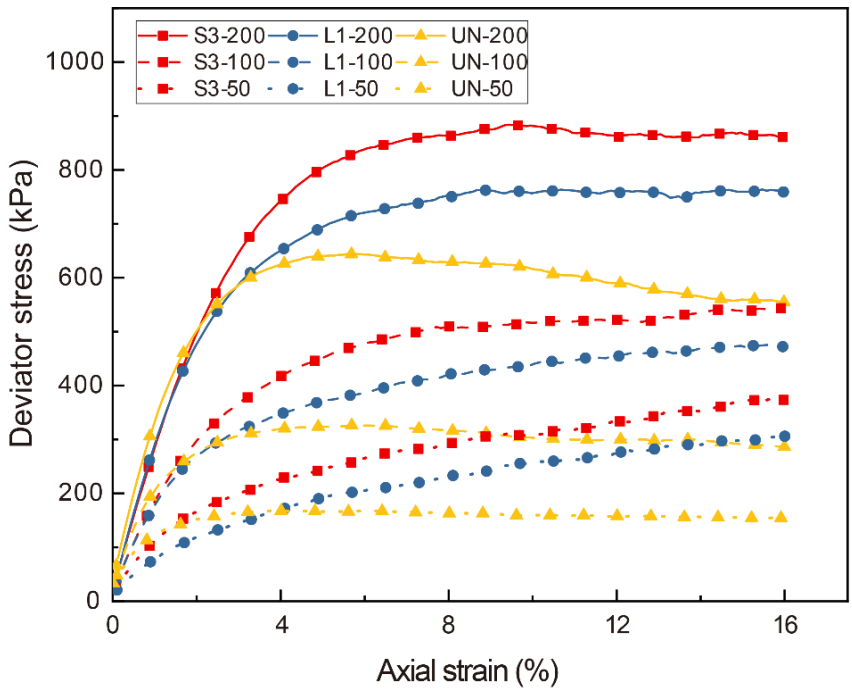

Fig. 9 Evolution of deviator stress for different reinforcement conditions

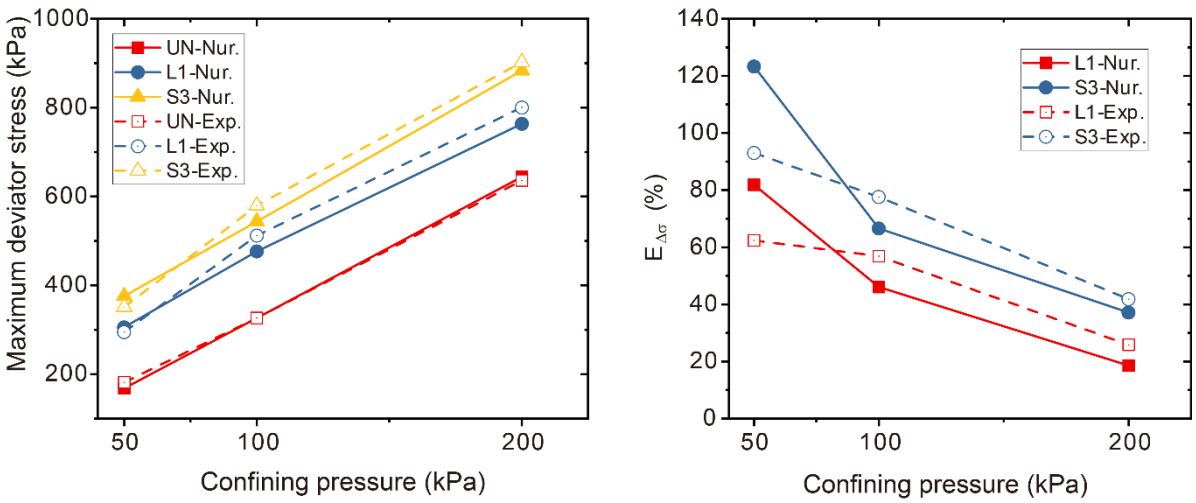

Fig. 10 Evolution of the (a) maximum deviator stress; (b) deviator stress increasing rate

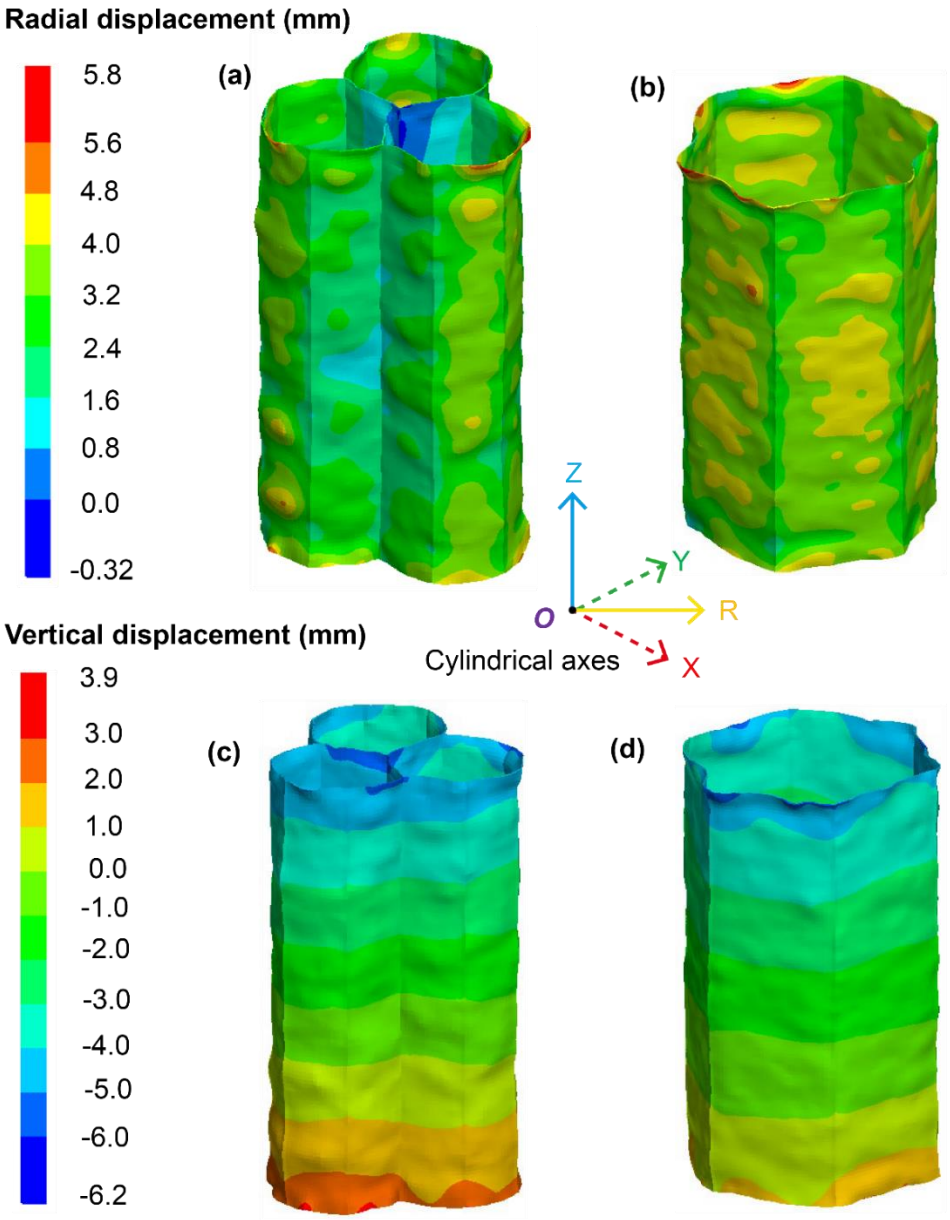

Fig. 11 Deformation of the geocells under confining pressure of 50 kPa: (a) Radial displacement of S3; (b) Radial displacement of L1; (c)Vertical displacement of S3; (d) Vertical displacement of L1

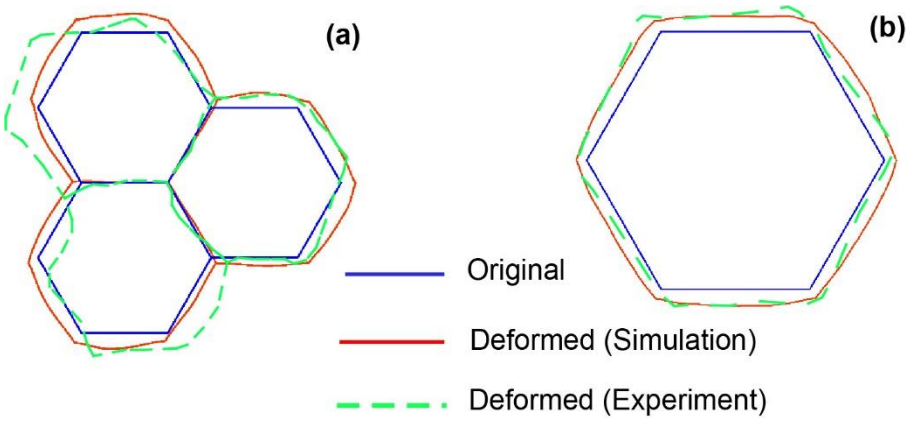

Fig. 12 Cross section contrast before and after deformation under confining pressure of 50 kPa: (a) S3; (b) L1

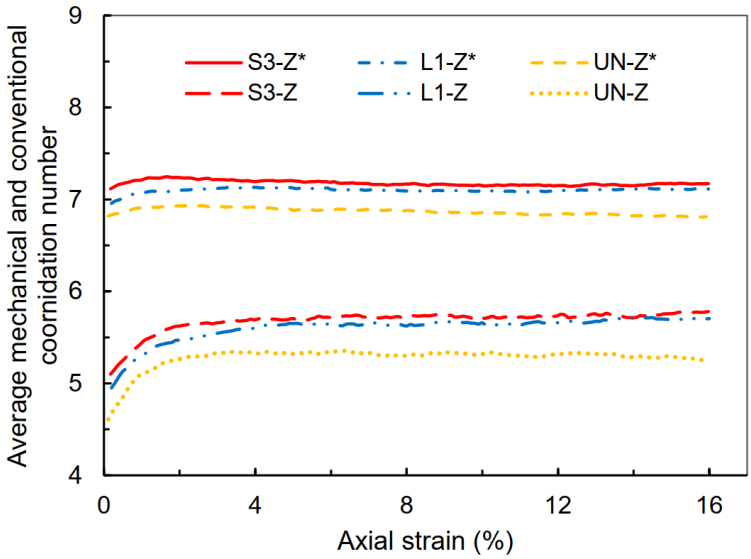

Fig. 13 Evolution of the average conventional and mechanical coordination number under confining pressure of 50 kPa

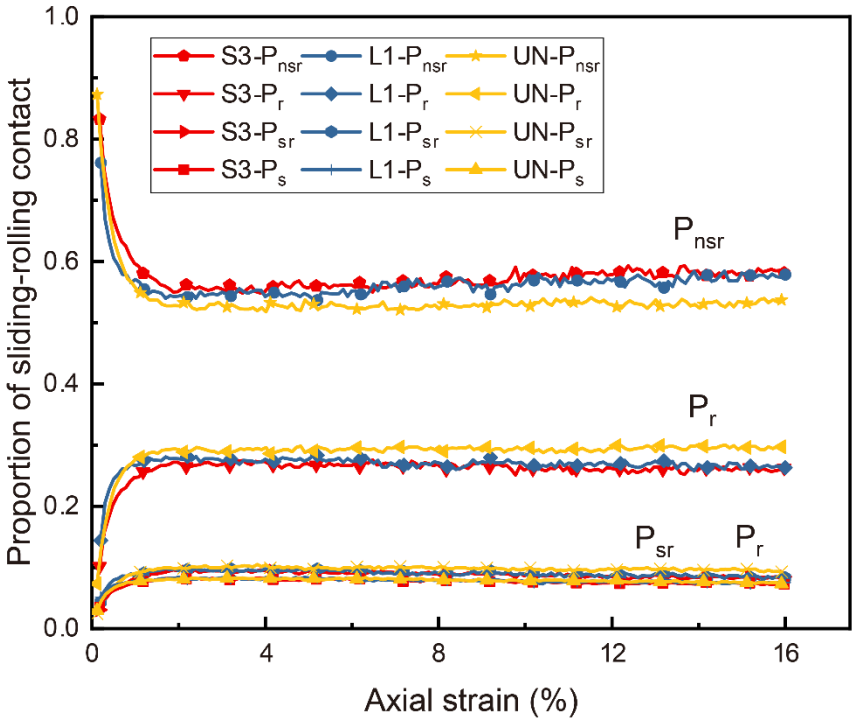

Fig. 14 Evolution of the sliding-rolling contact proportion under confining pressure of 50 kPa

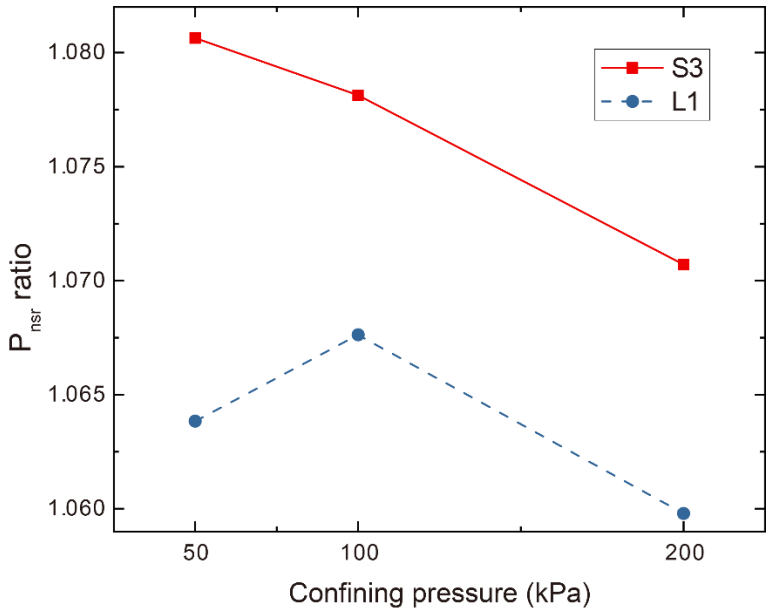

Fig. 15 Stable contact proportion ratio

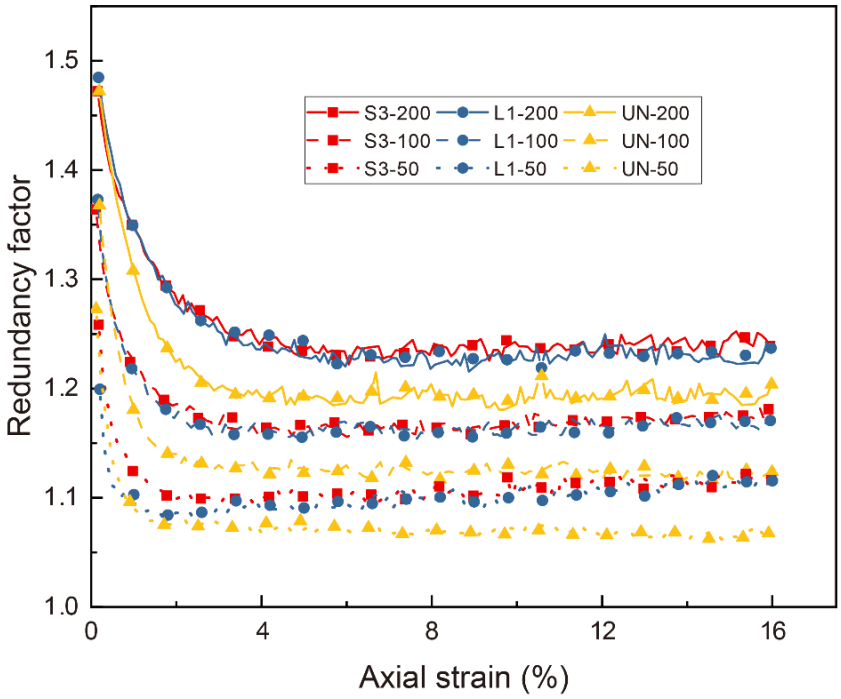

Fig. 16 Evolution of the RF for different reinforcement conditions

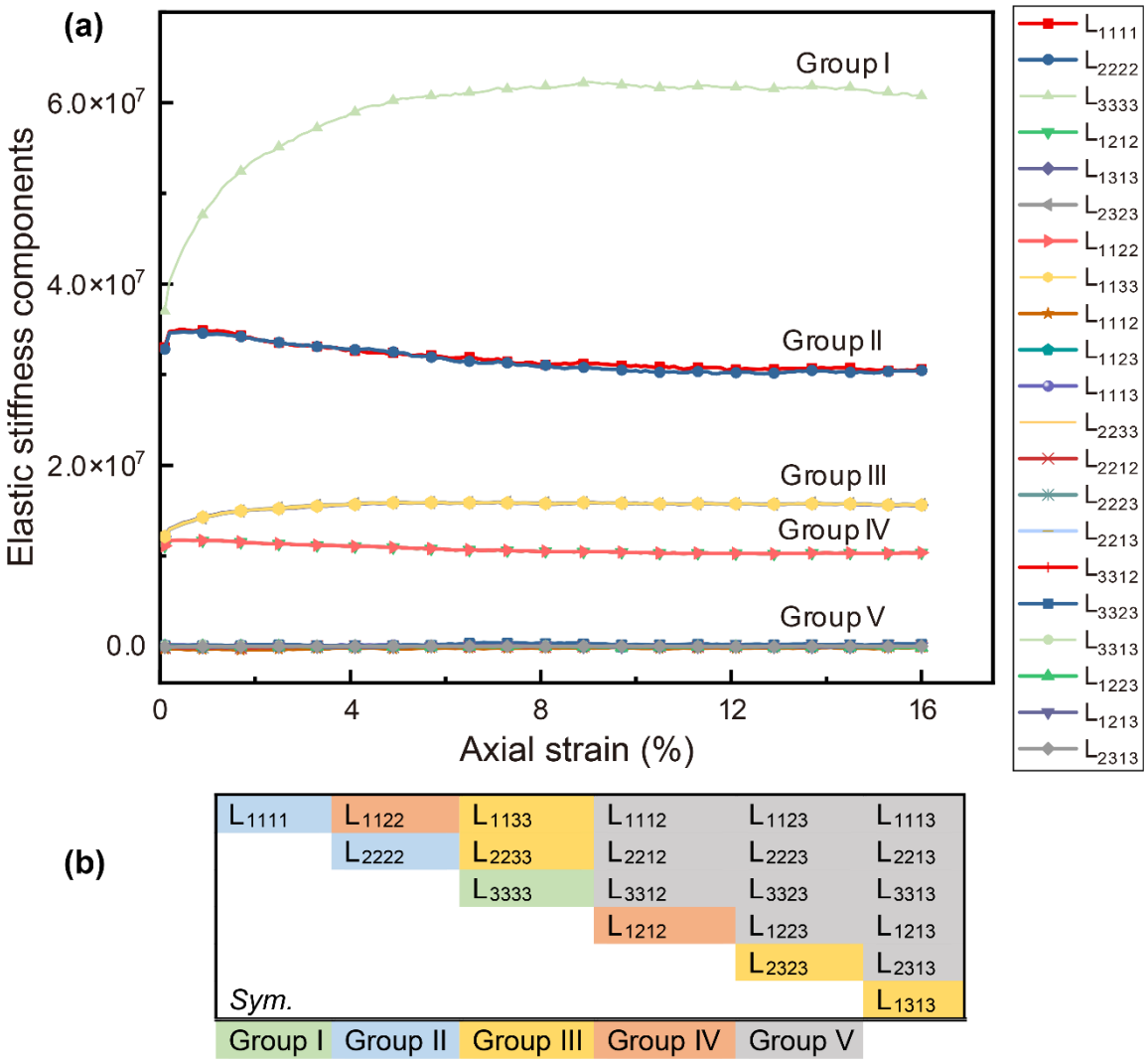

Fig. 17 Elastic stiffness tensor components: (a) evolution of the sample S3 under confining pressure of 50kPa; (b) group classification

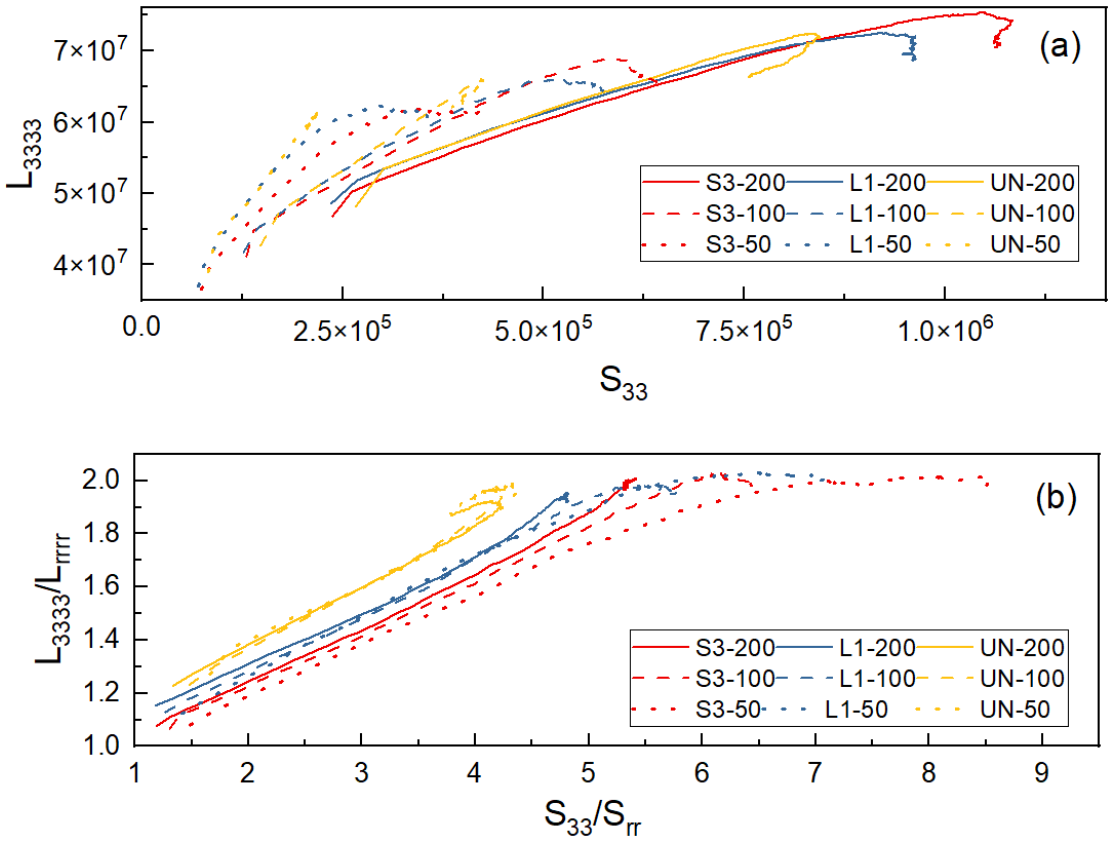

Fig. 18 (a) L_{3333} versus S_{33}; (b) principal elastic stiffness ratio (L_{3333}/L_{rrrr}) versus principal stress ratio (S_{33}/S_{11})

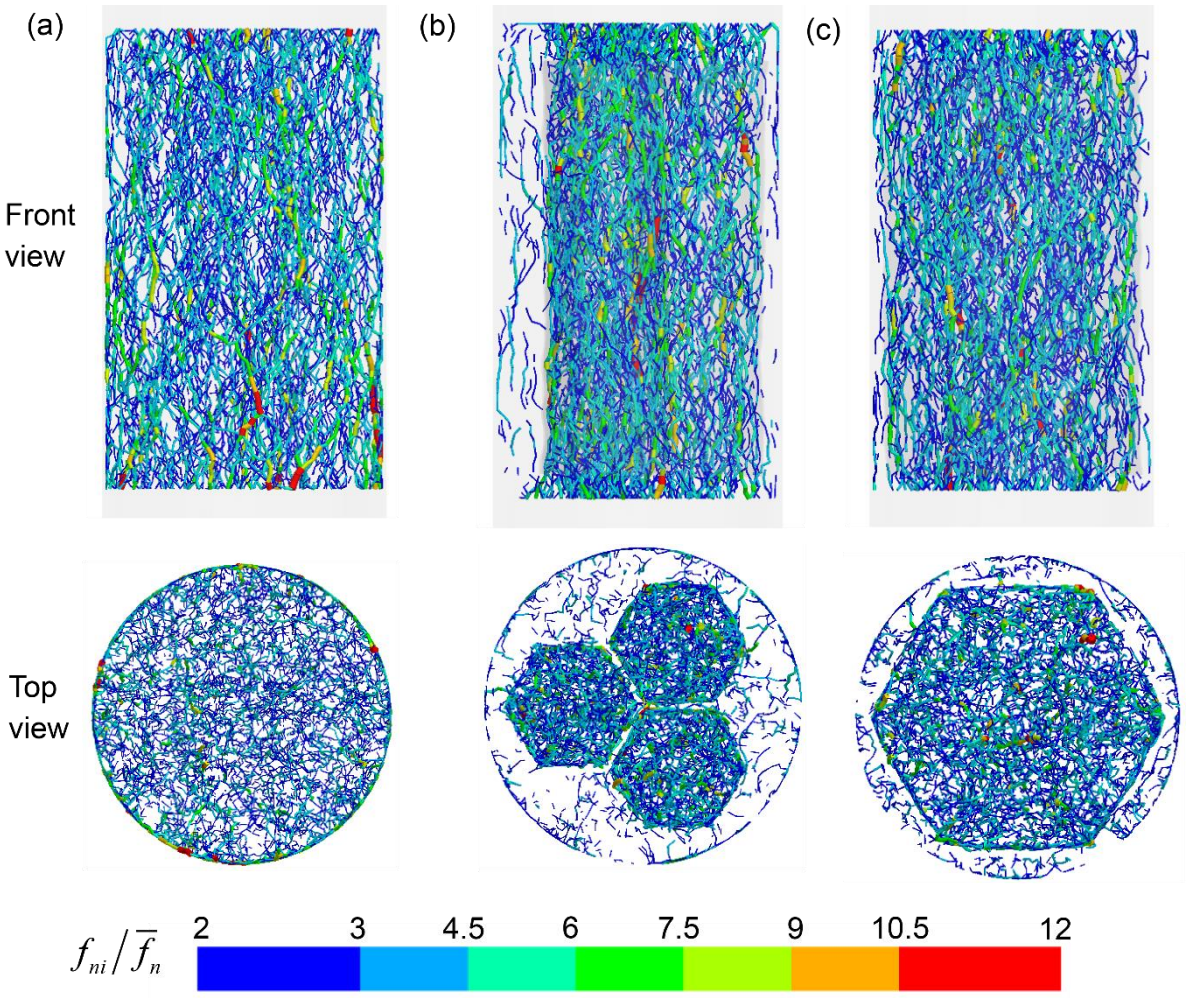

Fig. 19 Strong force chain network under confining pressure of 50 kPa:

(a) UN; (b) S3; (c) L1

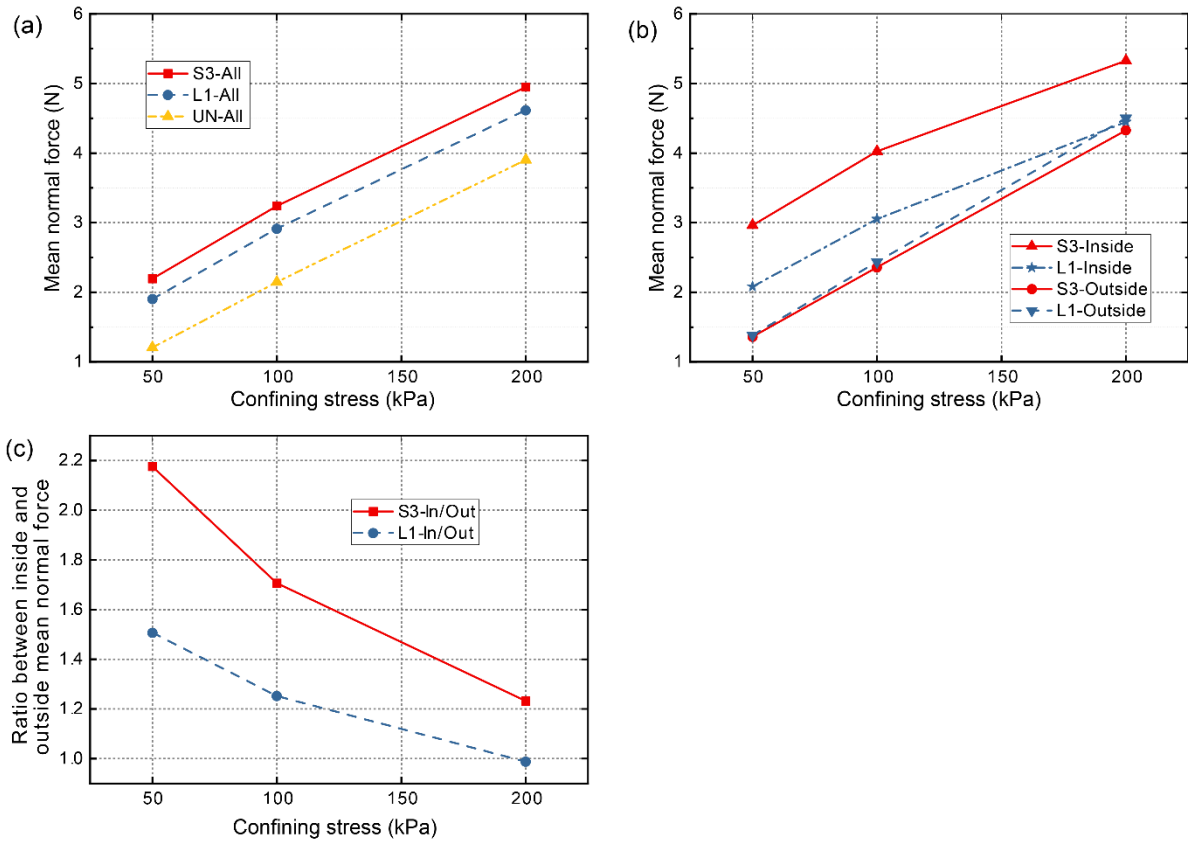

Fig. 20 Mean normal force contrast: (a) all; (b) inside and outside the geocell; (c) the ratio between the inside and outside mean normal force

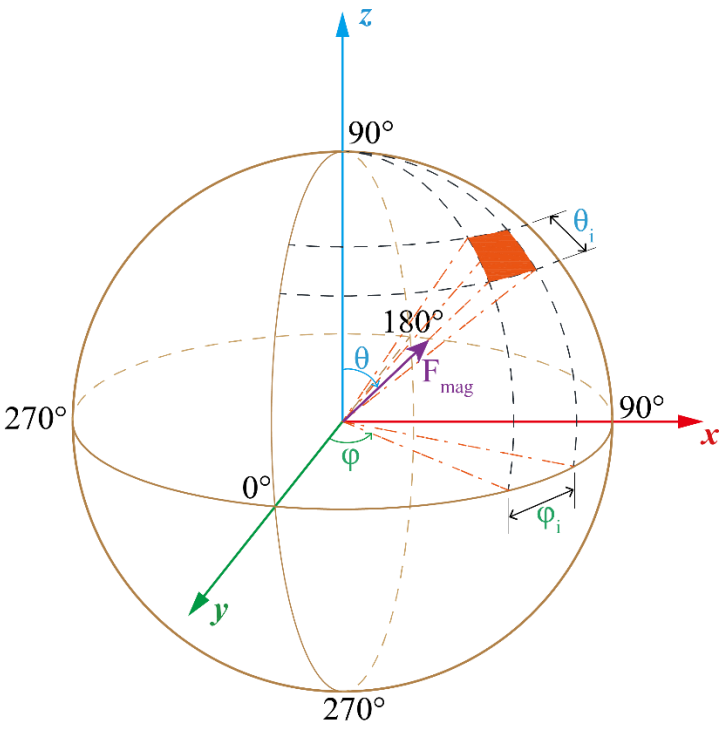

Fig. 21 Orientation grouping for the 3D histogram in the spherical coordinate system

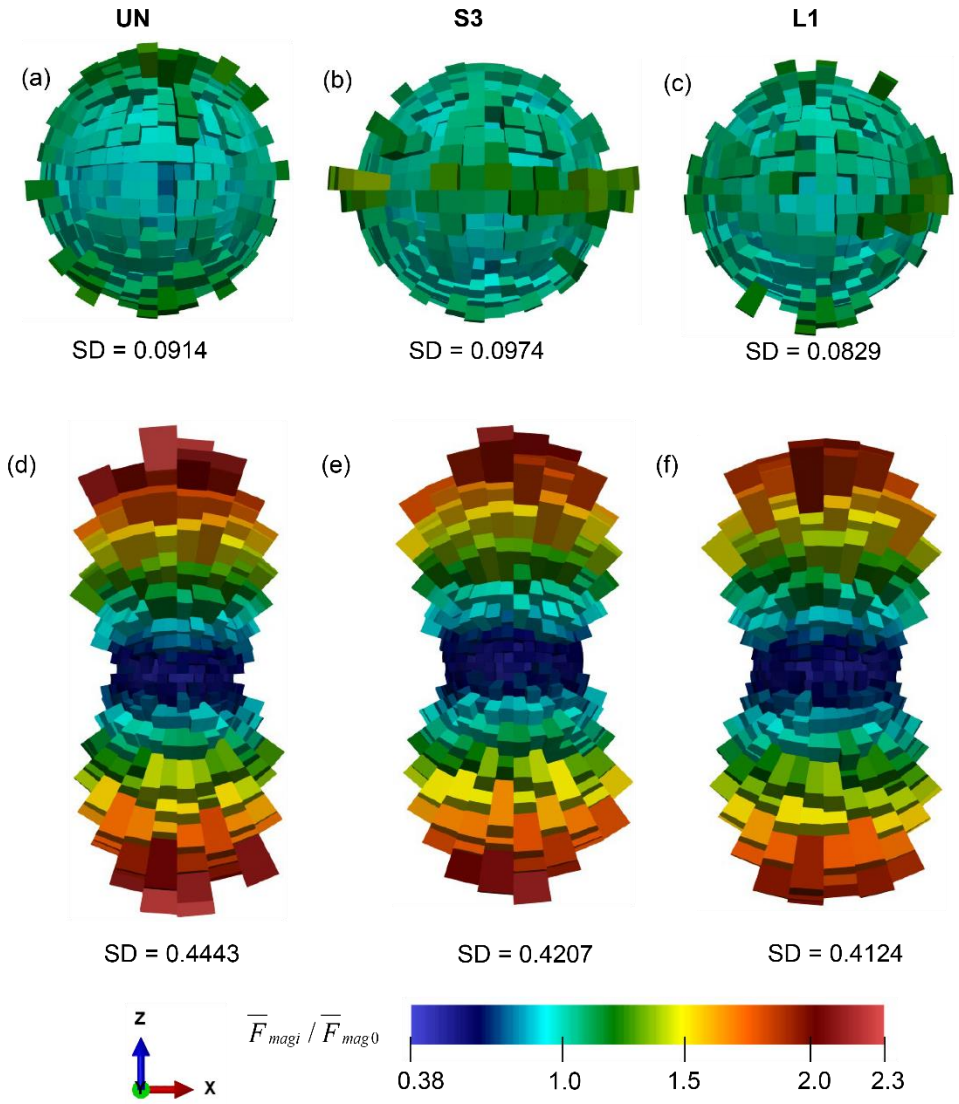

Fig. 22 3D histograms of the contact normal force magnitude in front view under confining pressure of 50 kPa at the initial state (a) UN; (b) S3; (c) L1; Final state: (d) UN; (e) S3; (f) L1

Table captions

Table 1 Micromechanical and material parameters used in the coupled FDM-DEM model

Table 2 Friction angle and apparent cohesion

Table 3 Contact classification based on sliding and rolling state

Table 1 Micromechanical and material parameters used in the coupled FDM-DEM model

Item	Micromechanical Properties
Discrete particles (balls)	
k_n (Particle-particle)	3.53×10^5 N/m
k_s (Particle-particle)	2.36×10^5 N/m
k_n (Particle-wall)	7.07×10^5 N/m
k_s (Particle-wall)	0
μ (Particle-particle)	0.6494
μ_r (Particle-particle)	0.5543
μ (Particle –wall)	0
Ball density	1550 kg/m^3
Continuous zones	
E	70.0 MPa
v	0.3

Table 2 Friction angle and apparent cohesion

Conditions	Apparent cohesion (kPa) C_r		Friction angle (°) φ		Additional confining stress (kPa) $\Delta\sigma_3$	
	Experiment	Simulation	Experiment	Simulation	Experiment	Simulation
UN	0	≈ 0	37	37.9	-	-
S3	44.2	47.2	39	39.1	58.8	62.8
L1	35.0	38.0	38	37.2	46.9	51.1

Table 3 Contact classification based on sliding and rolling state

Type	Symbol	Constraint	
		Quantity	Components
Sliding and rolling	C_{sr}	1	$F_{\hat{\boldsymbol{n}}_c}$
Only sliding	C_s	3	$F_{\hat{\boldsymbol{n}}_c}$, $M_{\hat{\boldsymbol{t}}_c}$, $M_{\hat{\boldsymbol{s}}_c}$
Only rolling	C_r	3	$F_{\hat{\boldsymbol{n}}_c}$, $F_{\hat{\boldsymbol{t}}_c}$, $F_{\hat{\boldsymbol{s}}_c}$
No sliding and rolling	C_{nsr}	5	$F_{\hat{\boldsymbol{n}}_c}$, $F_{\hat{\boldsymbol{t}}_c}$, $F_{\hat{\boldsymbol{s}}_c}$, $M_{\hat{\boldsymbol{t}}_c}$, $M_{\hat{\boldsymbol{s}}_c}$